

# The QUEST–La Silla AGN Variability Survey: selection of AGN candidates through optical variability

P. SÁNCHEZ-SÁEZ,<sup>1,2</sup> P. LIRA,<sup>1</sup> R. CARTIER,<sup>3</sup> N. MIRANDA,<sup>4</sup> L. C. HO,<sup>5,6</sup> P. ARÉVALO,<sup>7</sup> F. E. BAUER,<sup>8,9,10</sup> P. COPPI,<sup>11</sup>  
AND C. YOVANINIZ<sup>1</sup>

<sup>1</sup>*Departamento de Astronomía, Universidad de Chile, Casilla 36D, Santiago, Chile*

<sup>2</sup>*European Southern Observatory, Casilla 19001, Santiago 19, Chile*

<sup>3</sup>*Cerro Tololo Inter-American Observatory, National Optical Astronomy Observatory, Casilla 603, La Serena, Chile*

<sup>4</sup>*Institut für Informatik, Humboldt-Universität zu Berlin, 10099 Berlin, Germany*

<sup>5</sup>*Kavli Institute for Astronomy and Astrophysics, Peking University, Beijing 100871, China*

<sup>6</sup>*Department of Astronomy, School of Physics, Peking University, Beijing 100871, China*

<sup>7</sup>*Instituto de Física y Astronomía, Facultad de Ciencias, Universidad de Valparaíso, Gran Bretaña No. 1111, Playa Ancha, Valparaíso, Chile*

<sup>8</sup>*Instituto de Astrofísica and Centro de Astroingeniería, Facultad de Física, Pontificia Universidad Católica de Chile, Casilla 306, Santiago 22, Chile*

<sup>9</sup>*Millennium Institute of Astrophysics (MAS), Nuncio Monseñor Sótero Sanz 100, Providencia, Santiago, Chile*

<sup>10</sup>*Space Science Institute, 4750 Walnut Street, Suite 205, Boulder, Colorado 80301*

<sup>11</sup>*Yale Center for Astronomy and Astrophysics, 260 Whitney Avenue, New Haven, CT 06520, USA*

## ABSTRACT

We present our variability–based active galactic nuclei (AGN) selection technique. We used data from the QUEST–La Silla AGN variability survey to construct light curves for 208,583 sources over  $\sim 70$  deg<sup>2</sup>. Each light curve has at least 40 epochs and a length greater than or equal to 200 days. We used different variability features to characterize our light curves, and we implemented a Random Forest (RF) algorithm to classify our objects as either AGN or non–AGN according to their variability features and optical colors. We tested four classifiers, one that only includes variability features (RF1), one that includes variability features and also  $r - i$  and  $i - z$  colors (RF2), one that includes variability features and also  $g - r$ ,  $r - i$ , and  $i - z$  colors (RF3), and another that only includes optical colors. We trained our classifiers using a sample of spectroscopically confirmed AGN and stars. We obtained a sample of high probability candidates (hp–AGN) for each classifier, with 5,941 sources for RF1, 5,252 sources for RF2, 4,482 sources for RF3, and 18,821 sources for RF4. We divided each hp–AGN sample according to their  $g - r$  colors, defining blue ( $g - r \leq 0.6$ ) and red sub–samples ( $g - r > 0.6$ ). We confirmed the nature of some of our candidates using ancillary data, finding that most of the candidates known from the literature belong to the blue sub–samples. In order to test the efficiency of our technique we performed spectroscopic follow–up, confirming the AGN nature of 44 among 54 observed sources (81.5% of efficiency). From the campaign we concluded that the best classifier is RF2, since it provides the purest sample of AGN candidates. For the RF2 classifier, we confirmed 100% and 79.4% of the blue and red candidates, respectively. There is a high fraction of atypical AGN in the red sub–sample, with four broad absorption–line quasars, eight low–luminosity AGN (faint sources with optical continuum dominated by the host galaxy), and seven high–redshift AGN ( $z_{\text{spec}} > 2.5$ ).

*Keywords:* galaxies: active - methods: statistical - surveys

## 1. INTRODUCTION

Active galactic nuclei (AGN) are one of the most energetic phenomena in the universe and are characterized by time–variable emission in every waveband in which they have been studied. Variability studies are fundamental to understanding the extreme physical conditions of accretion disks near supermassive black holes (SMBH). Recent studies indicate that AGN vari-

ability can be well described as a stochastic process (e.g., damped harmonic oscillator or random walk; Kelly et al. 2009, 2014), with characteristic time–scales ranging from days to years.

The Large Synoptic Survey Telescope (LSST; Ivezić et al. 2008) will revolutionize time–domain astronomy, providing for the first time the opportunity to study variable objects for a long–period of time ( $\sim 10$  years),

at very faint magnitudes ( $r \sim 24.5$  for single images), and with a large total covered area ( $>18,000 \text{ deg}^2$ ). Simulations performed by the LSST AGN Science Collaboration predict detection of over  $10^7$  AGN to beyond  $r \sim 24$  (LSST Science Collaboration et al. 2009). This is a huge increase in the number of sources available for variability analysis since current studies typically only probe to limiting magnitudes of  $r \sim 21$ , with total number of sources between 10 and  $10^5$  (e.g. Cristiani et al. 1997; Vanden Berk et al. 2004; MacLeod et al. 2010; Peters et al. 2015; Simm et al. 2016; Caplar et al. 2017; Li et al. 2018). Given the ubiquity of variability and the large number of variable sources to be found with LSST, it is critical to characterize AGN variability and define reliable selection criteria before LSST enters in operations.

Traditionally, AGN selection follows the philosophy of finding regions in UV/optical/mid-IR color-color space in which AGN can be cleanly separated from stars and galaxies (e.g. Schmidt & Green 1983; Fan 1999; Richards et al. 2002; Lacy et al. 2004; Stern et al. 2005; Smith et al. 2005; Richards et al. 2009; Ross et al. 2012). However, some AGN populations have observed colors that fall outside the region occupied typically by bright, “blue” AGN, mimicking those of stars, such as type 2 or obscured AGN, broad absorption-line quasars (BAL-QSO), high-redshift quasars (high- $z$  QSO) (Butler & Bloom 2011; Palanque-Delabrouille et al. 2011), and low-luminosity AGN (LLAGN), whose colors can be highly contaminated by the emission from the host galaxy. Therefore, alternative methods to identify AGN candidates missed by traditional selection techniques are required, in order to obtain complete AGN samples. One promising selection method involves the use of variability techniques.

Butler & Bloom (2011) implemented a variability-based selection algorithm to classify high-redshift quasars in the Sloan Digital Sky Survey (SDSS; York et al. 2000) Stripe 82 field. They used damp random walk modelling (Kelly et al. 2009) to separate sources showing quasar-like variability from those with temporally uncorrelated variability. Particularly, they targeted sources with redshifts in the range  $2.5 \leq z \leq 3$ , where color-based selection of AGN is less efficient due to stellar contamination. Palanque-Delabrouille et al. (2011) used the variability structure function (e.g. Schmidt et al. 2010) to separate quasars, variable stars, and non-variable stars, in the SDSS Stripe 82 data. They implemented a neural network algorithm that separates the classes by their structure function parameters. A similar technique has been used by the SDSS IV *the extended Baryon Oscillation Spectroscopic*

*Survey* (eBOSS) team to select quasar candidates with  $z > 2.1$  by variability (Myers et al. 2015). Peters et al. (2015) used color, variability, and astrometric data from SDSS to select AGN candidates. They implemented a non-parametric Bayesian Classification Kernel Density Estimation (NBC KDE), to classify 35,820 type 1 quasar candidates in the Stripe 82 field. They tested various combinations of color and variability parameters, finding that using a combination of optical colors and variability parameters improves quasar classification efficiency and completeness over the use of colors alone. More recently, Tie et al. (2017) used data from the supernova fields of the Dark Energy Survey (DES; Abbott et al. 2018) to select quasars by combining color and variability selection methods. All these previous studies have shown the potential of selecting AGN candidates through variability analyses, demonstrating that variability-based techniques can increase considerably the number of AGN candidates in the redshift range where the colors of stars are similar to those of AGN. Less clear is how deep into the low-luminosity and obscured AGN populations they can probe. This is of substantial importance given the eventual mismatch that X-ray and MIR surveys will have compared with LSST.

In this paper we present our variability-based technique to select AGN candidates using data from the QUEST-La Silla AGN variability survey (Cartier et al. 2015). Variability features, like the structure function, have been used to characterize the variable sources (e.g. Cartier et al. 2015; Sánchez et al. 2017). We then used a Random Forest algorithm to classify our objects as either AGN or non-AGN. We tested four classifiers, one that includes only variability features, two that includes colors and variability features, and another one that includes only optical colors. The main difference of our selection technique with previous analyses is the use of light curves with higher cadence. Besides, we did not differentiate between point and extended sources during the classification. Hereby, we expect to detect more low-redshift AGN and LLAGN candidates than previous analyses. For some of our candidates we have obtained optical spectra to confirm their nature. Four of the fields observed by the QUEST-La Silla AGN variability survey correspond to the LSST Deep Drilling Fields (DDFs), whose expected cadence will be similar to the nightly cadence used by the QUEST-La Silla AGN variability survey (but extending the time baseline to 10 years)<sup>1</sup>. The QUEST-La Silla AGN variability

<sup>1</sup> <https://www.lsst.org/scientists/survey-design/ddf>

survey is an important test bed to study AGN selection in time-domain surveys, like LSST, or the Zwicky Transient Facility (ZTF, [Bellm 2014](#)), which has a depth similar to the QUEST–La Silla AGN variability survey.

The paper is organized as follows. In Section 2 we describe the QUEST–La Silla AGN variability survey, and the light curve construction procedure. In Section 3 we describe the Random Forest algorithm, the variability features, and the labeled set used for the selection. We also discuss the performance of our Random Forest classifiers, and we comment about the selected candidates. In Section 4 we provide the results on confirming the nature of some of our candidates by using public data and spectroscopic follow-up. In Section 5, we provide a comparison of our results with previous works. Finally, in Section 6 we summarize the main results.

## 2. DATA

### 2.1. The QUEST–La Silla AGN variability survey

Between 2010 and 2015 we carried out “The QUEST–La Silla AGN variability survey” (hereafter QUEST–La Silla), using the wide-field QUEST camera mounted on the 1m ESO-Schmidt telescope at La Silla Observatory ([Cartier et al. 2015, 2016](#)). The survey used a broad-band filter, the  $Q$  band, similar to the union of the  $g$  and  $r$  SDSS filters. Our survey includes the COSMOS, ECDF–S, ELAIS–S1, XMM–LSS and Stripe 82 fields. These are some the most intensively observed regions in the southern sky. Our QUEST fields are much larger than the nominal fields, but we will still adopt the same names, with a surveyed area of  $\sim 14 \text{ deg}^2$  per field, with the exception of the XMM–LSS field, which covers an area of  $\sim 38 \text{ deg}^2$ . One of the advantages of our survey over other surveys is the intense monitoring used, observing the fields every possible night (but see the binning strategy described below). Individual images reached a limiting magnitude between  $r \sim 20.5$  and  $r \sim 21.5 \text{ mag}$  for an exposure time of 60 seconds or 180 seconds, respectively.

The aims of our survey are: 1) to test and improve variability selection methods of AGN, and find AGN populations missed by other optical selection techniques ([Schmidt et al. 2010](#); [Butler & Bloom 2011](#); [Palanque-Delabrouille et al. 2011](#)); 2) to obtain a large number of well-sampled light curves, covering time-scales ranging from days to years; 3) to study the link between the variability properties (e.g., characteristic time-scales and amplitudes of variation) with physical parameters of the system (e.g., black-hole mass, luminosity, and Eddington ratio).

[Cartier et al. \(2015\)](#) presented the technical description of the survey, the full characterisation of the

QUEST camera, and a study of the relation of variability with multi-wavelength properties of X-ray selected AGN in the COSMOS field. In [Sánchez-Sáez et al. \(2018\)](#) we performed a statistical analysis of the connection between AGN variability and physical properties of the central SMBH, where we found that the amplitude of variability at one year time-scale ( $A$ ) depends primarily on the rest-frame emission wavelength ( $\lambda_{rest}$ ) and the Eddington ratio, where  $A$  anticorrelates with both  $\lambda_{rest}$  and  $L/L_{Edd}$ .

### 2.2. Light curve construction

We reduced the data from the QUEST–La Silla using our own customized pipeline, following the same procedure described by [Cartier et al. \(2015\)](#), which includes dark subtraction, flat-fielding, and astrometric and photometric calibration. To calibrate the photometry, we used public photometric SDSS catalogs ([Gunn et al. 1998](#); [Doi et al. 2010](#)) for the COSMOS, Stripe 82 and XMM–LSS fields, and public catalogs from the first year of DES ([Abbott et al. 2018](#)) for the ELAIS–S1 and ECDF–S fields. We performed aperture photometry using SExtractor ([Bertin & Arnouts 1996](#)), with the same optimal aperture found by [Cartier et al. \(2015\)](#) for the QUEST camera ( $\sim 6''.18$ ). We then constructed light curves for all the sources from the SDSS and DES catalogs with detections in the QUEST–La Silla data, using the same methodology as in [Cartier et al. \(2015\)](#). In summary, we constructed light curves by cross-matching the SDSS and DES catalogs with every QUEST–La Silla catalog, that we generated for each observation, for which we knew their associated Julian dates, using a radius of  $1''$ . We then constructed light curves for each source, keeping only those epochs where the SExtractor FLAG parameter was equal to zero, to prevent false detection of variability due to bad photometry. Finally, we only saved those light curves with more than three epochs. From the SDSS catalog, we could obtain single-epoch photometry of every source in the COSMOS, XMM–LSS, and Stripe 82 fields in the  $u$ ,  $g$ ,  $r$ ,  $i$ , and  $z$  bands, and from the DES catalog we obtained single-epoch photometry in the  $g$ ,  $r$ ,  $i$ , and  $z$  bands for the ELAIS–S1 and ECDF–S fields.

We decided to bin our light curves using three-day bins, in order to reduce the noise in our light curves produced by several factors, including changes in atmospheric conditions and the relatively low cosmetic quality of the QUEST CCD camera chips. This might effect the detection of variability of sources with short time-scale variations, like some variable stars (e.g. RR Lyrae or Cepheid stars), however, we do not expect to detect many variable stars in the QUEST–La Silla fields (e.g.

**Table 1.** Number of light curves per field.

Field	total light curves	well-sampled light curves
COSMOS	68,514	45,323
XMM-LSS	104,962	82,697
Elais-S1	49,504	38,106
ECDF-S	54,649	42,457
Total	277,629	208,583

Medina et al. 2018). Moreover, in this work we are focused in the detection of sources with long time-scale variations (with time-scales of months or years), thus the three-day binning does not affect our detection of AGN.

In this work, we excluded the Stripe 82 field, since it is a crowded field, and requires point spread function (PSF) photometry. We generated a total of 277,629 light curves for sources located in the COSMOS, ECDF-S, ELAIS-S1, and XMM-LSS fields. In order to have statistically significant variability features of the sources, we decided to include in our analysis only those light curves with at least 40 epochs and a length greater than or equal to 200 days, after the three days binning was applied (hereafter “well-sampled” light curves). There are 208,583 well-sampled light curves in the four fields. The median, mean and standard deviation of the number of epochs of each light curve are 118, 119.3, and 47.2, respectively; and the median, mean and standard deviation of the total length of each light curve are 1283.7, 1306.4, and 254.3, respectively. In Table 1 we summarize the total number of light curves and the number of well-sampled light curves in each field.

### 3. SELECTION OF AGN CANDIDATES

We implemented a supervised automatic classification using a Random Forest algorithm (RF; Breiman 2001) to classify our 208,583 objects with well-sampled light curves as either AGN or non-AGN according to their variability features and optical colors. We did not include a morphological parameter during the classification (e.g. SExtractor CLASS\_STAR parameter), in order to be able to detect sources with AGN-like variability with extended shapes. We tested four classifiers: one that includes only variability features, two that includes optical colors and variability features, and one that includes only optical colors. In the following sub-sections we describe the selection methodology, the features used in our analysis, and the results of the classification for sources from the QUEST-La Silla survey.

#### 3.1. Random Forests

A decision tree is a hierarchical structure that performs successive partitions on the data, each of them according to a certain criteria, such as a cut-off value in one of the descriptors or features. In this way, the data are divided into smaller and smaller subsets as the tree goes deeper, until it reaches the leaves of the tree. Each of the leaves is associated with a single class. A given class, however, may be associated with several leaves. Thus the elements that fall on any of the leaves corresponding to a particular class will be classified as belong to that class.

A RF algorithm consist of a collection single decision trees, where each tree is trained using a random sub-set of sources from a training set (a set of objects with known classification, selected from a labeled set). The final classification function of the algorithm weighs each of these results according to the size of the sub-set used by each tree, and generates an average score, which can then be interpreted as the probability that the input element belongs to a certain class (predicted class probability,  $P_{\text{RF}}$ ). Then, the classifier is validated using a sub-set of the labeled set that was not used to train (the test set). Finally, a prediction is made on the unlabeled data. RF has several advantages, it can handle thousands of features, it provides a ranking of feature importance during the classification, it does not need to scale the feature values to the same “units”, it handles numerous objects, and it is easily parallelizable.

For the selection of AGN candidates we used the *scikit-learn*<sup>2</sup> Python package implementation of RF. We performed a hyperparameter selection procedure in order to obtain the optimal values for the RF classifier, by means of a K-Fold Cross-Validation procedure (with 5 folds) and using the “accuracy” (see its definition in Section 3.4) as the target score to optimize. The parameters considered in this cross-validated search includes the number of trees in the forest, and the number of features to consider when looking for the best split in a tree. This hyperparameter selection procedure was executed as part of the model training phase (i.e. on the training set). In order to take into account the class imbalance in the classification process, we initialized the class weight hyperparameter as “*balanced\_subsample*”.

The variability features used by the RF classifier are described in the following section (3.2), and are listed in Table 2. We trained the RF classifier using a labeled set of type 1 AGN and stars with spectroscopic classification from SDSS and with well-sampled light curves from the QUEST-La Silla survey (see Section 3.3). During the

<sup>2</sup> <http://scikit-learn.org/stable/modules/generated/sklearn.ensemble.RandomForestClassifier.html>



RF classifier training, we used 70% of the labeled set as a training set, and then we tested the performance of the classifier using the remaining 30% of the labeled set (the test set), as normally done during supervised learning procedures. We then applied the trained RF classifier to our unlabeled set, composed by our 208,583 sources with well-sampled QUEST–La Silla light curves, to classify them as either AGN or non-AGN. As result, we obtain a predicted class and the predicted class probability ( $P_{\text{RF}}$ ) associated to each source of the unlabeled set.

### 3.2. Variability features

In order to have a complete description of the variability of our sources, we used several variability features. Following the same approach of [Sánchez et al. \(2017\)](#) and [Sánchez-Sáez et al. \(2018\)](#), we used two parameters related to the amplitude of the variability,  $P_{\text{var}}$  and the excess variance ( $\sigma_{\text{rms}}$ ), and one parameter that describes the shape of the variability between two observations separated by a given time, the structure function (SF).

In particular,  $P_{\text{var}}$  (see [Sánchez et al. 2017](#) and references therein) corresponds to the probability that the source is intrinsically variable; it considers the  $\chi^2$  of the light curve, and calculates the probability  $P_{\text{var}} = P(\chi^2)$  that a  $\chi^2$  lower or equal to the observed value could occur by chance for an intrinsically non-variable source.

$\sigma_{\text{rms}}$  is a measure of the intrinsic variability amplitude (see [Sánchez et al. 2017](#) and references therein), and it is calculated as  $\sigma_{\text{rms}}^2 = (\sigma_{\text{LC}}^2 - \bar{\sigma}_m^2) / \bar{m}^2$ , where  $\sigma_{\text{LC}}$  is the standard deviation of the light curve,  $\bar{\sigma}_m$  is the mean photometric error, and  $\bar{m}$  is the mean magnitude.

The SF (e.g. [Schmidt et al. 2010](#)) is the average variability amplitude between two observations separated by a given time ( $\tau$ ), and it can be modelled as a power-law:  $\text{SF}(\tau) = A_{\text{SF}} \left( \frac{\tau}{1\text{yr}} \right)^{\gamma_{\text{SF}}}$ , where  $A_{\text{SF}}$  corresponds to the amplitude of the variability at 1 year time-scale, and  $\gamma_{\text{SF}}$  is the logarithmic gradient of this change in magnitude.

We also used some variability features from the Feature Analysis for Time Series (FATS; [Nun et al. 2015](#)) Python package, related with the amplitude of the variability (e.g. the mean variance and the percent amplitude) and the structure of the light curve (e.g. the linear trend and the auto-correlation function length), as well as the period of the Lomb–Scargle periodogram ([VanderPlas 2018](#)), derived by using the AstroML module for Python ([VanderPlas et al. 2012](#)). A list of all the variability features used in this work is shown in Table 2, together with a brief description of each feature and its reference.

### 3.3. Labeled set

To train our RF classifier we need a labeled set, which has to be representative of the populations that we want to classify. Since in this analysis we only include extragalactic fields, we do not expect to detect a high fraction of variable stars, because of their low density at high Galactic latitudes (e.g. RR Lyrae or Cepheid stars, see [Medina et al. 2018](#) and references therein). Moreover, since we implemented a three-day binning to our light curves, the detection of variable signals with short-time scales is not possible. Therefore, any variable star with a short period will have a light curve that will not be very different from a non-variable star. Only variable stars with long periods would be detectable using our QUEST–La Silla light curves. We cross-matched the positions of the 208,583 sources with well-sampled light curves with the General catalogue of variable stars (Version GCVS 5.1, [Samus’ et al. 2017](#)), which provides a detailed compilation of catalogs of variable stars in the Galaxy. We found that only three known variable stars are present in our data, one RR Lyrae and two cataclysmic variables. Therefore, we did not include variable stars in our RF classifiers.

In this analysis, galaxies are not included in the labeled set, since in general their variability and color properties will be similar to those of stars, unless they host an AGN (which might not have been previously detected). Therefore, we constructed a labeled set composed by stars and type 1 AGN (i.e. AGN with broad permitted emission lines). We decided to include only type 1 AGN since we want to characterize properly the variability of the optical continuum emission, which cannot be detected in most of type 2 or obscured AGN.

Three of our fields (COSMOS, Stripe 82, and XMM–LSS) have spectroscopic information from SDSS. We constructed light curves for sources with spectral classification from the SDSS-DR14 database ([Abolfathi et al. 2018](#)). There are 3,313 type 1 AGN and 3,332 stars with at least three epochs in the QUEST–La Silla light curves, and 2,405 type 1 AGN and 2,608 stars with well-sampled light curves. We considered the sources with well-sampled light curves to define a labeled set for the RF classifier training. As mentioned in Section 3.1, 30% of the labeled set was used as a test set and 70% as training set for the RF modelling. Figure 1 provides examples of QUEST–La Silla light curves for four sources of the labeled set.

In Figure 2 we show three color–color diagrams of the labeled set:  $u-g$  vs  $g-r$ ,  $g-r$  vs  $r-i$ , and  $r-i$  vs  $i-z$ . As a reference, we mark the regions of the  $u-g$  versus  $g-r$  color–color diagram dominated by a particular type of source, from [Sesar et al. \(2007\)](#). We can see that a high fraction of the AGN in the labeled set are located in

**Table 2.** List of features.

Feature	Description	Reference
$P_{var}$	Probability that the source is intrinsically variable	McLaughlin et al. (1996)
$\sigma_{rms}$	Measure of the intrinsic variability amplitude.	Allevato et al. (2013)
$A_{SF}$	Amplitude of the variability at 1 year, derived from the SF	Schmidt et al. (2010)
$\gamma_{SF}$	Logarithmic gradient of the change in magnitude, derived from the SF	Schmidt et al. (2010)
Std*	Standard deviation of the light curve ( $\sigma_{LC}$ )	Nun et al. (2015)
Meanvariance*	Ratio of the standard deviation to the mean magnitude ( $\sigma_{LC}/\bar{m}$ )	Nun et al. (2015)
MedianBRP*	Fraction of photometric points within amplitude/10 of the median magnitude	Richards et al. (2011)
Autocor-length*	Lag value where the auto-correlation becomes smaller than $e^{-1}$	Kim et al. (2011)
StetsonK*	A robust kurtosis measure	Kim et al. (2011)
$\eta^{e*}$	Ratio of the mean of the square of successive differences to the variance of data points	Kim et al. (2014)
PercentAmp*	Largest percentage difference between either the max or min magnitude and the median	Richards et al. (2011)
Con*	number of three consecutive data points that are brighter or fainter than $2\sigma_{LC}$	Kim et al. (2011)
LinearTrend*	Slope of a linear fit to the light curve	Richards et al. (2011)
Beyond1Std*	Percentage of points beyond one $\sigma_{LC}$ from the mean	Richards et al. (2011)
Q31*	Difference between the third quartile and the first quartile of a light curve	Kim et al. (2014)
PeriodLS	Period from the Lomb–Scargle periodogram	VanderPlas (2018)

**Note.** (\*) Features from FATS

a region of the  $u-g$  vs  $g-r$  diagram where low-redshift, luminous AGN (II) are the dominant population, which corresponds to 78.8% of the AGN in the labeled set. This corresponds to the classical color-color selection of “blue” AGN. Moreover, we can see in the figure that several high-redshift ( $z_{spec} > 2.5$ ) AGN in the labeled sample are located in the region where high-redshift luminous AGN are the dominant component (VI), as expected, but a non negligible fraction is located in other regions, where binary stars or cool dwarf stars (III), RR Lyrae stars, and main sequence stars or “stellar locus” (V) are the dominant population. The true number density of these “non-classical” AGN are largely unknown, as they are hard to find.

On the other hand, we can see in the right panel of Figure 2 that most of the AGN in the labeled set are located in a region where  $r-i \lesssim 0.7$  and  $i-z \lesssim 0.8$ , cleanly isolating a sub-population of cool dwarf stars. This can be understood considering that stellar colors become monotonically redder as the effective temperature decreases (Covey et al. 2007), thus we normally observe a high concentration of cool dwarf stars in a region around  $g-r \sim 1.5$ , with  $r-i \gtrsim 0.8$ . Besides, extragalactic sources (i.e., galaxies and AGN) are normally located in regions of the color-color space with  $r-i \lesssim 1.0$  (e.g., Rahman et al. 2016), since their integrated emission typically has a low contribution from cool dwarf stars. Therefore, we can use  $r-i$  and  $r-z$  colors to separate AGN from cool dwarf stars. The sepa-

ration of AGN and stars from the general “stellar locus” is more complicated if we only use optical colors, since there is a high overlap between these two populations in the different color-color diagrams, particularly in the  $u-g$  vs  $g-r$  diagram, as already discussed. Thus, including variability information in the selection of AGN candidates will be extremely useful to improve AGN selection.

### 3.4. Performance of the Random Forest classifier

We tested four different RF classifiers. The first one includes only variability features (hereafter RF1). The second one includes variability features and the  $r-i$  and  $i-z$  colors (hereafter RF2). The third classifier includes variability features and the  $g-r$ ,  $r-i$ , and  $i-z$  optical colors (hereafter RF3). And the last classifier includes only the  $g-r$ ,  $r-i$ , and  $i-z$  optical colors (hereafter RF4). We exclude  $u-g$  since we do not have photometry in the  $u$  band for the Elais-S1 and ECDF-S fields, and because our labeled set does not cover properly the  $u-g$  space, compared to the unlabeled set, thus including it might produce poor results.

As can be seen, the difference between RF2 and RF3 is the exclusion of the color  $g-r$  in RF2. As we mentioned in the previous section, the  $r-i$  and  $i-z$  colors can easily separate cool dwarf stars and AGN. However, the separation of AGN and stars from the stellar locus is difficult when we use optical colors, particularly for the case of  $u-g$  and  $g-r$ . Thus, with RF2 we can

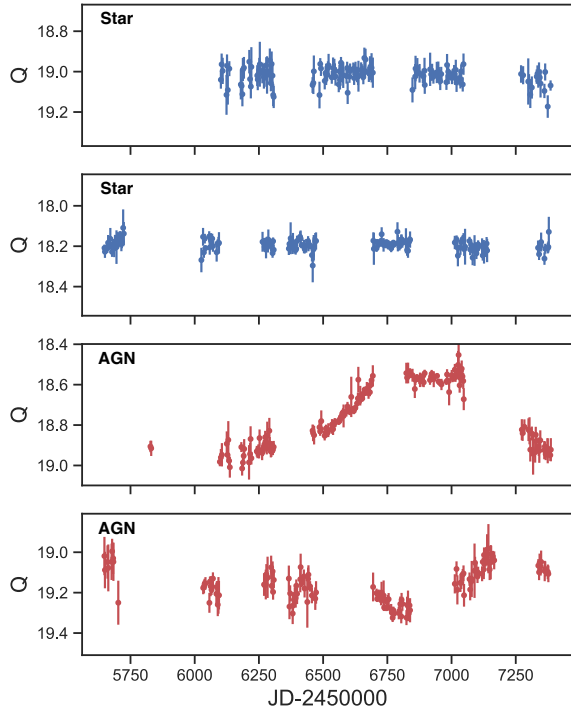


**Figure 1.** Example of four light curves from the QUEST–La Silla labeled set: two stars (blue dots, top panels) and two AGN (red dots, bottom panels).

test whether avoiding the use of  $g - r$  can improve the detection of redder AGN populations.

Since we are interested in select only AGN candidates, for the rest of the analysis we will refer to stars, and any source that is not an AGN as non-AGN.

#### 3.4.1. RF1: selection of AGN based solely on variability

Our first RF classifier (RF1) includes only variability features. We show the results from this classifier using a confusion matrix, which is shown in Figure 3 (see its RF1 results). It can be seen that AGN (true positives) are in general well classified, and also that the fraction of non-AGN classified as AGN (false positives) is very low.

We also computed the following scores to asses our classifiers: accuracy ( $A$ ), precision ( $P$ ), recall ( $R$ ), and F1. These scores are defined by means of the True Positives (TPs: known AGN classified as AGN by the RF classifier), the False Positives (FPs: known non-AGN classified as AGN), the True Negatives (TNs: known

**Table 3.** Scores measured in the test set for each classifier

Score	RF1	RF2	RF3	RF4
Accuracy	0.916	0.923	0.931	0.868
Precision	0.909	0.909	0.921	0.890
Recall	0.933	0.950	0.951	0.851
F1	0.921	0.930	0.936	0.870

non-AGN classified as non-AGN), and the False Negatives (FNs: known AGN classified as non-AGN):

$$\begin{aligned}
 A &= \frac{TPs + TNs}{Total\ Sample} \\
 P &= \frac{TPs}{TPs + FPs} \\
 R &= \frac{TPs}{TPs + FNs} \\
 F1 &= 2 \times \frac{P \times R}{P + R}
 \end{aligned} \tag{1}$$

Table 3 shows the computed scores for the RF1 classifier. From these scores, and from the confusion matrix, we can say that RF1 presents a low fraction of False Positives, thus, the sample of predicted AGN has low contamination from non-AGN. However, we tend to miss a fraction of real AGN ( $\sim 10\%$ ). This results from the difficulty of detecting a variable signal from AGN with low amplitude variability, and since we are only considering variability properties for the classification, they could be classified as non-AGN.

It is important to consider that we are testing the RF1 classifier in a sample of AGN selected mostly by means of their optical colors, and since we are only considering variability features in our selection, the confusion matrix and the different scores, obtained from our labeled sample, might not necessarily be an optimal prediction of the performance of our method in the unlabeled sample.

One of the advantages of the RF classification is that we can easily know the feature importance, since it provides a ranking score for each feature, or how well every feature separates the two classes. In the first columns of Table 4, we provide the list of features, ordered by importance (rank value), for the RF1 classifier. It can be seen that the four most important features are the amplitude of the structure function, the excess variance, the Meanvariance, and Q31. In Figure 4, we show the distribution of the  $A_{SF}$  and Q31 features for the labeled set. We highlight using black dots those AGN classified as variable, according to the definition proposed by Sánchez et al. (2017), where a source is classified as variable when its light curve satisfies  $P_{var} \geq 0.95$  and

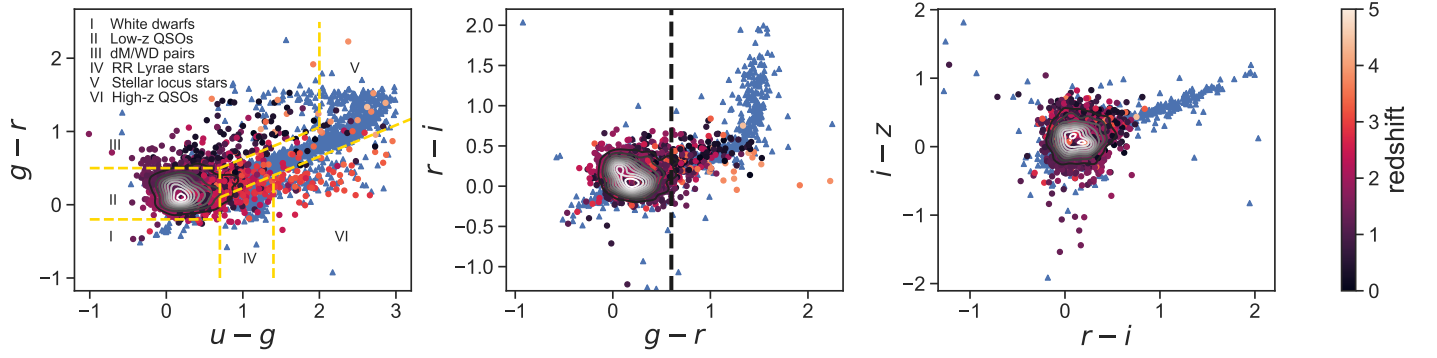


**Figure 2.** Color-color diagrams of the labeled set. In the left panel we show  $u - g$  versus  $g - r$ , in the middle panel  $g - r$  vs  $r - i$ , and in the right panel  $r - i$  vs  $i - z$ . The stars are represented by blue triangles, and the AGN are represented by circles whose colors depend on the redshift of each source. The contour plots show the distribution of AGN. In the left panel we show with yellow dashed lines the division used in [Sesar et al. \(2007\)](#) to identify regions of the  $u - g$  versus  $g - r$  diagram dominated by a particular type of source. In the middle panel, the black dashed line shows the position where  $g - r = 0.6$ .

True Label	AGN	RF1: 0.90 RF2: 0.89 RF3: 0.91 RF4: 0.89	RF1: 0.10 RF2: 0.11 RF3: 0.09 RF4: 0.11
	NON-AGN	RF1: 0.07 RF2: 0.05 RF3: 0.05 RF4: 0.15	RF1: 0.93 RF2: 0.95 RF3: 0.95 RF4: 0.85
		AGN	NON-AGN
		Predicted Label	

**Figure 3.** Confusion matrix from testing the RF1, RF2, RF3, and RF4 classifiers in the test set. True Label represent the classification done from SDSS spectra, and Predicted Label is the outcome of each classifier.

$(\sigma_{rms}^2 - err(\sigma_{rms}^2)) > 0$ . From the figure, it can be seen that AGN and non-AGN are separated by these two features, with  $A_{SF}$  providing a much stronger division than Q31, as there is substantial source overlap between the two classes with the latter indicator. It can be also seen that the majority of the AGN with low variability amplitude are classified as non-variable.

### 3.4.2. RF2: selection of AGN based on variability and $r - i$ , and $i - z$ optical colors

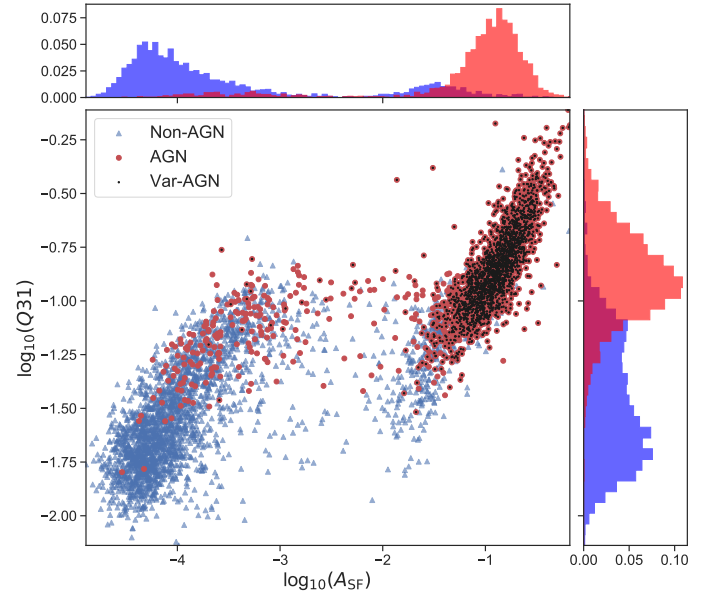


**Figure 4.** Distribution of the  $A_{SF}$  and Q31 features for the labeled set. Blue triangles correspond to non-AGN, and red circles correspond to AGN. We mark with black dots those AGN classified as variable, according to the definition used in [Sánchez et al. \(2017\)](#).

Our second RF classifier (RF2) includes variability features and the  $r - i$  and  $i - z$  colors. Figure 3 shows the confusion matrix for RF2 (see its RF2 results). In this case, the confusion matrix is similar to the confusion matrix of RF1, however, in the case of RF2 we have a slightly cleaner population of AGN candidates (i.e. the fraction of False Positives is lower). The accuracy, precision, recall, and F1 scores are given in Table 3. There



**Table 4.** Feature importance for each classifier.

RF1		RF2		RF3		RF4	
Feature	Rank	Feature	Rank	Feature	Rank	Feature	Rank
$A_{\text{SF}}$	0.197	$A_{\text{SF}}$	0.209	$A_{\text{SF}}$	0.189	$g - r$	0.436
$\sigma_{\text{rms}}$	0.139	$\sigma_{\text{rms}}$	0.149	$\sigma_{\text{rms}}$	0.142	$r - i$	0.304
Meanvariance	0.127	Q31	0.102	Q31	0.113	$i - z$	0.260
Q31	0.111	$P_{\text{var}}$	0.093	Meanvariance	0.099		
$P_{\text{var}}$	0.095	Std	0.088	$P_{\text{var}}$	0.095		
Std	0.090	Meanvariance	0.086	Std	0.074		
PercentAmp	0.040	PercentAmp	0.045	Autocor-length	0.042		
$\gamma_{\text{SF}}$	0.036	Autocor-length	0.035	PercentAmp	0.039		
Autocor-length	0.033	$\gamma_{\text{SF}}$	0.031	$g - r$	0.031		
MedianBRP	0.025	$r - i$	0.028	$\gamma_{\text{SF}}$	0.029		
LinearTrend	0.023	MedianBRP	0.021	$r - i$	0.023		
PeriodLS	0.023	PeriodLS	0.020	MedianBRP	0.020		
$\eta^e$	0.023	$\eta^e$	0.019	$\eta^e$	0.020		
Beyond1Std	0.019	Beyond1Std	0.019	$i - z$	0.019		
StetsonK	0.018	LinearTrend	0.019	LinearTrend	0.018		
Con	0.002	$i - z$	0.019	PeriodLS	0.017		
		StetsonK	0.014	Beyond1Std	0.017		
		Con	0.002	StetsonK	0.012		
				Con	0.002		

are not significant differences between the score values of RF1 and RF2.

In Table 4 we list the ranking of features for the RF2 classifier. There are not significant differences when compared to RF1, and notably we found that variability features are more relevant for AGN selection than the  $r - i$  and  $i - z$  colors. In this case, the most important features are  $A_{\text{SF}}$ ,  $\sigma_{\text{rms}}$ , Q31, and  $P_{\text{var}}$ . We also found that the  $r - i$  color seems to be more relevant than the  $i - z$  to classify our sources.

#### 3.4.3. RF3: selection of AGN based on variability and $g - r$ , $r - i$ , and $i - z$ optical colors

Our third RF classifier (RF3) includes variability features and the  $g - r$ ,  $r - i$ , and  $i - z$  colors. Figure 3 shows the confusion matrix for RF3 (see its RF3 results). In this case, the fraction of True Positives (True AGN classified as AGN) is slightly higher than those of RF1 and RF2. However, we must consider that most of the AGN in the labeled set have been selected by means of their optical colors, which might explain the improvement of the results over the test set compared with the RF2 classifier.

The scores for RF3 are listed in Table 3. In comparison to RF1 and RF2, the scores are slightly higher, particularly the precision. In Table 4 we list the ranking of features for the RF3 classifier. In this case the most

important features are  $A_{\text{SF}}$ ,  $\sigma_{\text{rms}}$ , Q31, and the Meanvariance. The most important color is  $g - r$ , which is expected due the distribution of non-AGN and AGN in Figure 2.

#### 3.4.4. RF4: selection of AGN based on optical colors

The last classifier (RF4) includes only the  $g - r$ ,  $r - i$ , and  $i - z$  optical colors. In Figure 3 we show its confusion matrix (see its RF4 results). In this case, the fraction of False Positives (Non-AGN classified as AGN) is higher. This can be explained by the overlap of non-AGN and AGN colors in some locations of the color-color spaces. The scores of RF4 are also listed in Table 3. They are lower than those of RF1, RF2, and RF3. In Table 4 we show the ranking of features for RF4. It can be seen that  $g - r$  is the most important color for the selection of AGN in the labeled sample.

We must consider that this color selection is not similar to other AGN optical color selections previously done (e.g. Richards et al. 2002), which have been mostly based in color cuts, similar to those shown in Figure 2. In addition, there is a non negligible fraction of AGN in the labeled set located in regions of the color-color spaces where different stellar populations are the dominant component, thus, as mentioned in Section 3.3, it is difficult to separate AGN and stars using only optical

colors. This might explain the low performance of the RF4 classifier compared with the other three classifiers.

### 3.5. AGN candidates from QUEST-La Silla

We applied the trained RF1, RF2, RF3, and RF4 classifiers to our unlabeled well-sampled set of 208,583 light curves. In order to improve the purity of our selection, we considered the predicted class probability  $P_{\text{RF}}$  (computed as the mean predicted class probabilities of the trees in the forest) to select the final set of AGN candidates. We defined two samples of AGN candidates: a) the full-AGN sample, consisting of all sources classified as AGN by the RF classifier ( $P_{\text{RF}} \geq 0.5$ ), and b) the hp-AGN sample, consisting in sources that have a high probability ( $P_{\text{RF}} \geq 0.8$ ) of being an AGN based on the RF classifier. In Table 5 we provide a summary with the number of sources classified as AGN in both samples, for each classifier. For the case of the RF1 classifier, there are 17,120 sources in the full-AGN sample, and 5,941 sources in the hp-AGN sample. For the RF2 classifier there are 15,100 sources in the full-AGN sample, and 5,252 sources in the hp-AGN sample. For RF3, there are 13,810 sources in the full-AGN sample, and 4,482 sources in the hp-AGN sample. Finally, for the RF4 classifier, there are 47,694 sources in the full-AGN sample, and 18,821 sources in the hp-AGN sample. There are 2,306 candidates in common between the RF1, RF2, RF3, and RF4 hp-AGN samples. For the rest of the analysis we will only consider the hp-AGN samples of each classifier.

Figure 5 shows the  $g-r$  vs  $r-i$  color-color diagram of the unlabeled set, and the hp-AGN samples for the RF1, RF2, RF3, and RF4 classifiers. Comparing with Figure 2, we can see that several of our AGN candidates are located in regions of the color-color space where AGN are not normally found, particularly for the case of RF1. The main difference between the candidates of RF1 and the rest of the classifiers, is the exclusion of sources in the color-color region where we normally find cool stars. For example, there are 4,890 candidates in common between RF1 and RF2, and 1,051 RF1 candidates that are not candidates for RF2. 54.1% of the former ones have  $r-i > 0.7$ , where we expect to find mostly cool stars. The main differences between the candidates of RF2 and RF3, is the exclusion of the redder candidates in the case of RF3 ( $g-r \gtrsim 1.0$ ). There are 4,178 candidates in common between RF2 and RF3, and 1,074 candidates in RF2 that are not candidates for RF3, with 70.5% of these having  $g-r > 1.0$ . Moreover, the number of candidates for the RF4 classifier is significantly higher compared with the other three classifiers, with more than three times the number of candidates of RF1,

RF2, or RF3. It is clear from Figure 5 that the performance of RF4 is poor, since this classifier only includes optical colors, but it is still selecting a high fraction of candidates in locations of the color-color space where stars are the dominant component. We believe that this is produced by difficulty of separating AGN and stars from the stellar locus when we only use optical colors (as we discussed in Section 3.3).

In the top-left panel of Figure 5 we also show a selection of AGN candidates observed during spectroscopic follow-up (see Section 4.2). In the top-right and bottom-left panels of the figure we show the position in the  $g-r$  vs  $r-i$  diagram of four candidates located in different positions of the stellar locus, marked with letters (ABCD), and in Figure 9 we show their light curves, where it can be seen that they are clearly variable. These four sources are selected as candidate by RF1, two are selected as candidates by RF2 (A and B), and none of them is selected as candidate by RF3 and RF4.

## 4. CONFIRMATION OF AGN CANDIDATES

In the following sub-sections, we aim to confirm the nature of our candidates. In Section 4.1, we use ancillary data to confirm the nature of our AGN candidates. In Section 4.2 we show the results of our spectroscopic follow-up campaign, conducted between December 2016 and September 2018, to test the efficiency of our selection method.

We are particularly interested in identifying the nature of sources located in positions of the color-color space dominated by stars (e.g. in the stellar locus). We divided our high probability candidates according to their  $g-r$  colors, we avoid  $u-g$  since the  $u$  band is not available for all the fields. We define the blue sub-sample as the one composed of sources with  $g-r \leq 0.6$  and the red sub-sample as that composed of sources with  $g-r > 0.6$ . As can be seen in Figure 2, most of the AGN in the labeled set have  $g-r \leq 0.6$ .

### 4.1. Confirmation by ancillary data

The Million Quasars Catalog (MILLIQUAS v5.7 update<sup>3</sup>, 7 January 2019, Flesch 2015) provides a very complete compendium of known AGN (both type 1 and type 2), from the literature, including the last data release of SDSS (SDSS-DR15), and several recent XMM-Newton, Swift, and Chandra catalogs (e.g. Evans et al. 2014; Marchesi et al. 2016; Maitra et al. 2019). It also in-

<sup>3</sup> <https://heasarc.gsfc.nasa.gov/W3Browse/galaxy-catalog/milliquas.html>

**Table 5.** Number of AGN candidates per field, for each classifier

Field	RF1		RF3		RF2		RF4	
	full-AGN	hp-AGN	full-AGN	hp-AGN	full-AGN	hp-AGN	full-AGN	hp-AGN
COSMOS	3,968	1,503	3,562	1,201	3,424	1,018	11,745	4,847
XMM-LSS	6,441	2,374	5,774	2,106	5,516	1,879	29,688	12,548
Elais-S1	3,374	988	2,936	942	2,441	777	3,278	712
ECDF-S	3,337	1,076	2,828	1,003	2,429	808	2,983	714
Total	17,120	5,941	15,100	5,252	13,810	4,482	47,694	18,821

cludes a list of high-confidence AGN candidates from different sources like AllWISE (Secrest et al. 2015).

We used MILLIQUAS to confirm the nature of our candidates. We cross-matched MILLIQUAS with the coordinates of our well-sampled light curves, using a radius of  $1''$ . There are 3,524 sources in the well-sampled sample with identifications in MILLIQUAS. For the case of the RF1 classifier, there are 2,358 (66.9%) of these sources in the hp-AGN sample, 2,757 (78.2%) in the full-AGN sample, and 767 (21.8%) sources classified as non-AGN. For the RF2 classifier, there are 2,366 (67.1%) sources in the hp-AGN sample, 2775 (78.7%) in the full-AGN sample, and 749 (21.3%) sources classified as non-AGN. For the RF3 classifier, there are 2,348 (66.7%) sources in the hp-AGN sample, 2,769 sources in the full-AGN sample (78.6%), and 755 (21.4%) sources classified as non-AGN. Finally, for the RF4 classifier, there are 2,285 (64.8%) sources in the hp-AGN sample, 3,123 (88.6%) sources in the full-AGN sample, and 401 (11.4%) sources classified as non-AGN. From these results we can say that  $\sim 21\%$  of the sources are misclassified as non-AGN when we include variability features in the selection. Thus, we can conclude that when we include variability features in our selection, we obtain a completeness of  $\sim 79\%$ .

We plot in the top panel of Figure 7 the distribution of the  $A_{SF}$  variability feature, for sources in MILLIQUAS and QUEST-La Silla belonging to the RF1 hp-AGN sample, the RF1 full-ANG sample, and sources classified as non-AGN by RF1 (but classified as AGN by MILLIQUAS). It can be seen that the main difference between the sources classified as AGN and non-AGN is the value of the variability amplitude at one year, i.e. we are not detecting variability for the sources classified as non-AGN.

In the middle panel of Figure 7 we compare the distribution of the mean  $Q$  magnitude (determined from their light curves) of sources from the RF1 hp-AGN sample that have and do not have detection in MILLIQUAS, and in the bottom panel we compare their  $A_{SF}$  distributions. It can be seen that the sources with detection

in MILLIQUAS are in general brighter than the sources without detection in MILLIQUAS, however the amplitude of the variability is lower for the sources without detection in MILLIQUAS. This tell us that when we include variability we improve the detection of faint candidates.

In Table 6 we show the number of hp-AGN candidates confirmed using MILLIQUAS, dividing the hp-AGN samples into red and blue sub-samples, as already described. It can be seen that most of the confirmed sources are in the blue sub-sample, with 52% of the candidates in this sample confirmed for RF1, 52.4% for RF2, 52.1% for RF3, and 19.5% for RF4. For the case of the red sub-sample, 5.3% of the candidates from RF1 are confirmed using MILLIQUAS, 7.1% for RF2, 12% for RF3, and 1.6% for RF4. Besides, there are 354 AGN listed as candidates in MILLIQUAS for RF1, 356 for RF2, 345 for RF3, and 336 for RF4. Most of them are candidates from WISE (Secrest et al. 2015).

#### 4.1.1. Candidates with X-ray detections

MILLIQUAS provides X-ray detections associated to every source, however some recent catalogs like Luo et al. (2017) Chen et al. (2018) are not completely included. Thus, we used different X-ray catalogs to complement the information provided by MILLIQUAS and see which candidates have X-ray detections associated. For the COSMOS field we used the optical and infrared counterparts catalog of the Chandra COSMOS-Legacy Survey (Marchesi et al. 2016), for the XMM-LSS field we used the recent XMM-SERVS survey catalog (Chen et al. 2018), for the ECDF-S field we used the Chandra Deep Field-South 7 Ms source catalog (Luo et al. 2017), and for the Elais-S1 field we used Elais-S1 field X-ray source optical/IR Identifications catalog (Feruglio et al. 2008).

In table 6 we provide the number of candidates with X-ray detections from the previously mentioned X-ray catalogs or MILLIQUAS (see the row "X-ray detections"). It can be seen that most of the candidates with X-ray detections are from the blue sub-sample.

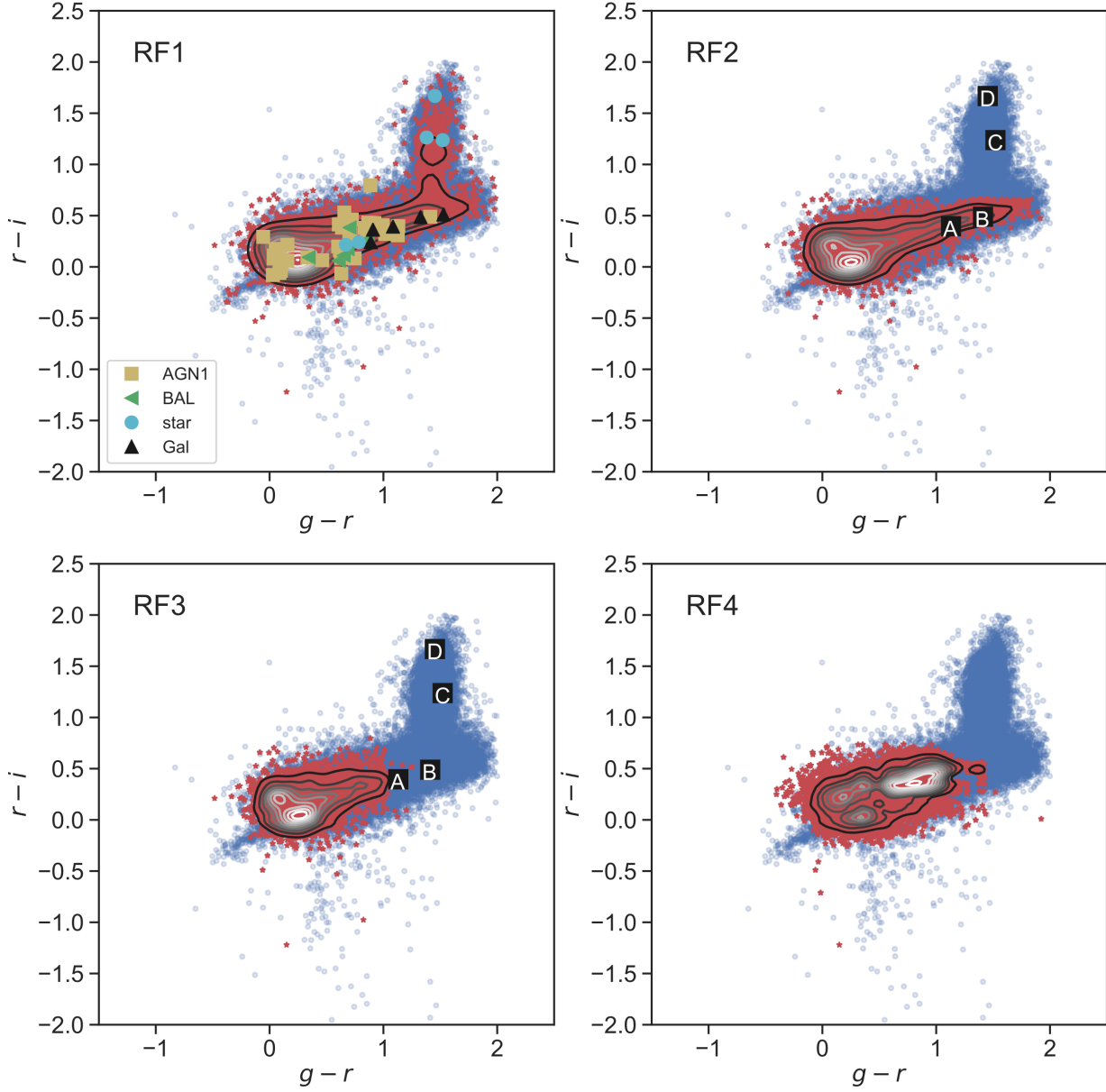


**Figure 5.**  $g-r$  vs  $r-i$  color-color diagrams of the unlabeled set (blue circles), and the hp-AGN sample (red stars) for the RF1 (top-left panel), RF2 (top-right panel), RF3 (bottom-left panel), and RF4 (bottom-right panel). The contour plots show the distribution of the hp-AGN samples for each classifier. In the top-left panel, we show the position of candidates observed during spectroscopic follow-up, differentiating between type 1 AGN (AGN1, yellow squares), BAL-QSO (BAL, red triangles), stars (cyan circles), and galaxies (Gal, black triangles). In the top-right and bottom-left panels we show with letters and black squares the position of a selection of observed candidates located in the stellar locus.

#### 4.2. Spectroscopic follow-up of AGN candidates

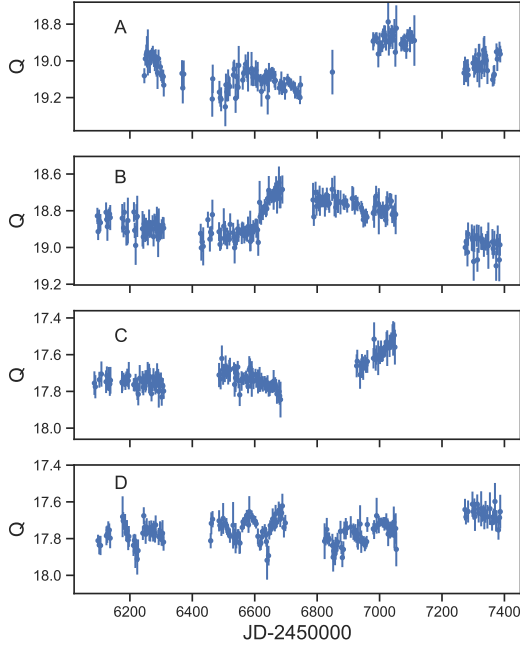
Since most of the AGN confirmed with ancillary data have blue colors ( $g-r \leq 0.6$ ), we performed spectroscopic follow-up to confirm the nature of sources located in different regions of the color-color space. We used Goodman at SOAR (Clemens et al. 2004) and EFOSC2 at NTT (Buzzoni et al. 1984) instruments to observe 54 candidates (for details see Section B of the appendix).

To select the candidates for the follow-up campaign we divided the hp-AGN sample of the RF1 classifier into the blue and red sub-samples. Then, we randomly selected 100 candidates from each sub-sample, excluding sources with  $r > 20.5$  for which it would be hard to obtain a good-quality spectra with 4-meter class telescopes. We visually inspected the light curves of the selected candidates in order to exclude sources with ev-



**Table 6.** Number of hp-AGN candidates confirmed using MILLIQUAS, for each classifier

Sample	RF1		RF2		RF3		RF4	
	blue	red	blue	red	blue	red	blue	red
MILLIQUAS AGN	1,882	122	1,894	116	1,901	100	1,787	158
MILLIQUAS candidate	324	30	322	34	320	25	286	50
X-ray detections	640	59	644	57	641	47	586	87
hp-AGN	3,618	2,323	3,613	1,639	3,646	836	9,164	9,657

**Figure 6.** Light curves of some RF1 candidates located in the stellar locus, observed during the spectroscopic follow-up campaign, shown in the top-right and bottom-left panels of Fig. 5. A and B are classified as type 1 AGN, C and D are classified as M-type stars.

idence of bad photometry (produced by the relatively low cosmetic quality of the QUEST CCD camera chips). During the follow-up campaign we observed as much of the selected candidates as we could, observing in total 54 targets. We gave priority to sources from the red sub-sample, of the 54 candidates observed, 38 have  $g - r > 0.6$ , which represents 70% of the sample.

In the top panel of Figure 8 we show the  $r$  band magnitude distribution of hp-AGN candidates of the RF1 classifier and the observed candidates. We can see that the distributions are different. This is produced by the limitations of observing faint targets with 4-meter class

telescopes. During the follow-up campaign we gave priority to sources with  $r < 20$ , for which we expected to obtain spectra with signal to noise higher than 10. In the bottom panel of Figure 8 we show the distribution of the predicted class probability ( $P_{RF}$ ) for the hp-AGN candidates of the RF1 classifier and the observed candidates. It can be seen that in general we observed sources with higher probabilities, compared with the total sample of candidates. This is produced by the visual inspection of the light curves and the selection of brighter sources for the follow-up campaign.

We used the spectra to classify our targets and to estimate their redshifts. For details about the spectroscopic analysis see section B of the appendix. The full list of observed candidates can be found in Section A of the appendix. We provide the position of the observed sources, their redshift, their  $g - r$  and  $r - i$  colors, their  $r$  magnitude, and their spectroscopic classification. In Table 7 we provide a summary of the follow-up campaign. We divided the classified sources into blue and red sub-samples, and we also separate them according to their spectroscopic classes: AGN1 (type 1 AGN), BAL-QSO, galaxy, and star.

In the top-left panel of Figure 5, we show the color-color diagram of the observed candidates, with colors and shapes depending on their spectral classification. In the top-right and bottom-left panels of Figure 5 we mark with letters some candidates located in the stellar locus. The sources A and B are classified as type 1 AGN, and the sources C and D are classified as type M stars. From the light curves of sources C and D (see Figure 9) and from their spectra, we propose that these candidates are irregular variable stars.

In the bottom panel of Figure 8 we show the normalized redshift distribution of AGN from the labeled sample, and observed candidates classified as AGN or BAL-QSO. We can see that we have a much larger fraction of low-redshift sources observed during the follow-up campaign. Besides, the fraction of observed AGN with  $z > 3.0$  is slightly higher compared with the AGN from the labeled sample.

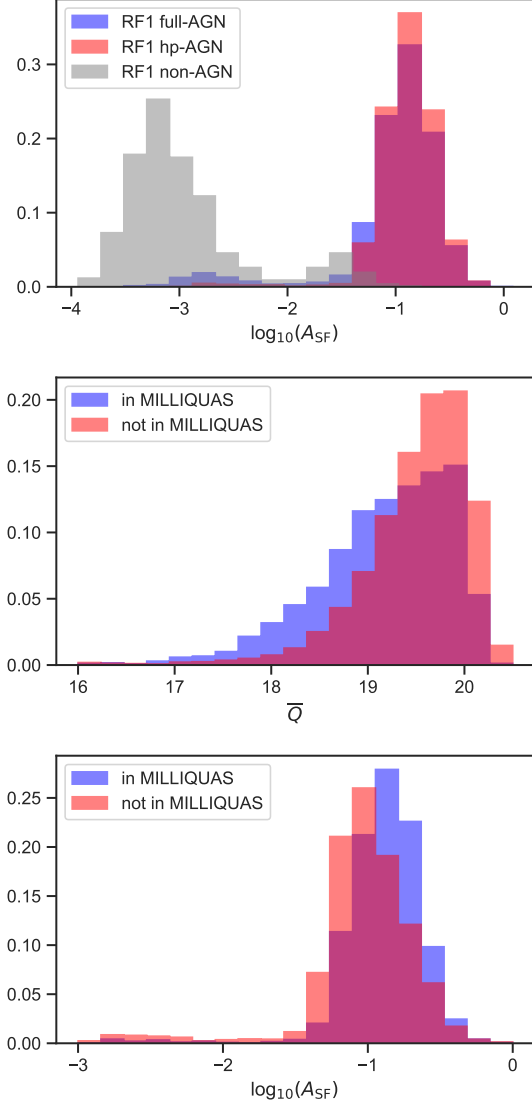


**Figure 7.** Top panel: normalized distribution of  $A_{SF}$  for sources with detection in MILLIQUAS with well-sampled light curves in QUEST–La Silla. We show sources from the RF1 full-AGN sample (blue), the RF1 hp-AGN sample (red), and sources classified as non-AGN by RF1. Middle panel: normalized distribution of the mean  $Q$  magnitude for sources from the hp-AGN sample that are present (blue) and not present (red) in MILLIQUAS. Bottom panel: normalized distribution of  $A_{SF}$  for sources from the hp-AGN sample that are present (blue) and not present (red) in MILLIQUAS. 5.

There are seven targets with redshift higher than 2.5. These types of AGN are hard to detect using typical color-color selections, and clearly benefit from the variability criteria (Palanque-Delabrouille et al. 2011; Butler & Bloom 2011). In addition, we found four BAL-QSO, with three having  $g - r > 0.6$ . There are 22 AGN with

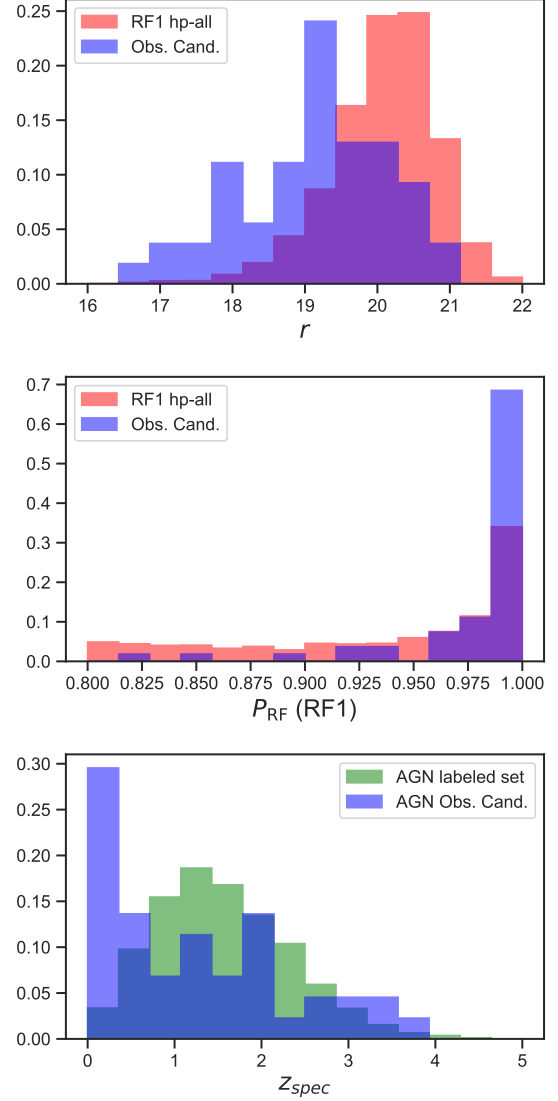


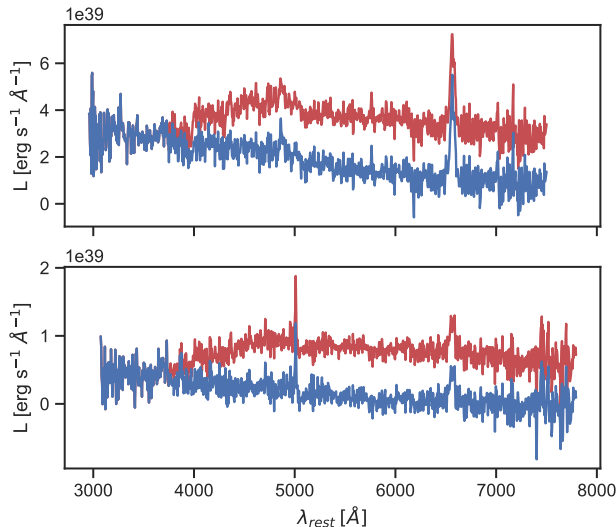
**Figure 8.** Top panel: normalized histogram of the  $r$  band magnitude of the RF1 hp-AGN sample (red) and the observed candidates (blue). Middle panel: normalized histogram of the predicted class probability ( $P_{RF}$ ) of the RF1 hp-AGN sample (red) and the observed candidates (blue). Bottom panel: normalized histogram of spectroscopic redshift of AGN from the labeled sample (green) and observed candidates classified as type 1 AGN or BAL-QSO (red).

$z_{spec} < 0.7$ , of which 20 have  $g - r > 0.6$ , and eight of these are LLAGN, whose continua are significantly dominated by the host galaxy, but with clearly distinguishable broad emission lines.

The case of the eight LLAGN is particularly interesting, since the continuum of their spectra is dominated by the host galaxy, but we still detect its optical variable component, which is associated with the accretion disk.

**Table 7.** Summary of the spectroscopic follow-up campaign

Class	blue sub-sample	red sub-sample	Total
AGN1	15	25	40
BAL-QSO	1	3	4
Galaxy	0	5	5
Star	0	5	5

**Figure 9.** Rest-frame optical spectra of two type 1 AGN with evidence of continuum dominated by the host galaxy (LLAGN), observed with EFOSC2/NTT. In red we show the original spectra, and in blue we show the AGN component. The most prominent emission lines correspond to  $H\alpha$ .

This component is revealed by subtracting the galactic continuum of each spectrum following the simple procedure of [Greene & Ho \(2005\)](#) and [Kim et al. \(2006\)](#). As an example, in Figure 9 we show the spectra of two LLAGN sources, in red we show the original observed spectra and in blue we show the AGN component. It can be seen that in both cases the continuum is dominated by the host galaxy, but after its subtraction, the power-law AGN continuum appears, which is the one that produces the optical variations. It is important to remark that without including variability features in the selection of our candidates, these type of sources would be classified as non-AGN according to their optical colors. This reflects the importance of including variability in the selection of different AGN populations.

We define the efficiency of a classifier as the number of confirmed AGN divided by the total number of observed

candidates. Considering all the observed candidates, the efficiency is 100% for the blue sub-sample, and 73.7% for the red sub-sample. In Table 8 we show from which classifier comes every observed candidate. As we mentioned previously, the 54 observed candidates belong to the RF1 hp-AGN sample, therefore the efficiency of the follow-up for the RF1 classifier is 100% for the blue sub-sample, and 73.7% for the red sub-sample. For the case of RF2, there are 50 observed candidates, with an efficiency of 100% for the blue sub-sample and 79.4% for the red sub-sample. There are three stars and one type 1 AGN excluded by RF2. For the case of RF3, there are 43 observed candidates. The efficiency of the RF3 blue sub-sample is 100% and for the red sub-sample is 85.2%. There are four type 1 AGN, one BAL-QSO, three galaxies, and three stars excluded by RF3. For the case of RF4, there are 17 observed candidates, 12 from the blue sub-sample, and five from the red sub-sample. All of them are type 1 AGN, thus the efficiency in this case is 100% for both sub-samples. There are 37 observed sources excluded by RF4, with 33 of them belonging to the red sub-sample. There are five stars, five galaxies, four BAL-QSO, and 23 type 1 AGN excluded by RF4.

From these results, we can conclude that RF2 is a better classifier. This is because it has a high efficiency for both the blue and red sub-samples, and exclude most of the observed stars and only one type 1 AGN. RF3 also provides good results, however it excluded one BAL-QSO and four type 1 AGN, of which one has  $z_{spec} = 3.5852$ , and two are LLAGN. In Section C we provide the list of hp-AGN candidates from the RF2 classifier.

#### 4.2.1. Non-AGN observed sources

We observed 10 sources which were spectroscopically classified as stars or galaxies, but as AGN by our classifiers; all of which have clear evidence of variability. These 10 sources are selected as candidates by RF1, seven are selected as candidates by RF2 (two star and five galaxies), four are selected as candidates by RF3 (two stars and two galaxies), and none of them is selected as candidate by RF4.

For the galaxy-classified cases, the light curves show clear signs of AGN-like variability. The obtained spectra of these sources are generally noisy (signal to noise less than 10), so we could be missing some weak emission lines. We tried to subtract a galactic component from these sources, and in some cases we found evidence of a power-law continuum component, but without evidence of emission lines. We decided to classify this sources as galaxies, however, in order to confirm their true nature, we likely need deeper observations, using 8-meter class

telescopes. We note that [Cartier et al. \(2015\)](#) found that about 20% of the objects classified spectroscopically as galaxies showed variability, they found a similar percentage of narrow-line AGN showing variability.

For the star-classified cases, four of them are M-type stars, and one seems to be a K-type star. From their light curves, we can conclude that they are semi-periodic or irregular variable stars.

## 5. COMPARISON WITH PREVIOUS WORKS

[Butler & Bloom \(2011\)](#) used SDSS photometry to select AGN candidates through variability in the Stripe 82 field. They used damp random walk modelling ([Kelly et al. 2009](#)) to detect quasar-like variable sources. The light curves used in their analysis have on average 10 epochs, with a maximum of 28, obtained over  $\sim 6$  years ([Sesar et al. 2007](#)). As can be seen in Figure 8 of [Butler & Bloom \(2011\)](#), most of their candidates lie in the region where typical AGN are found, and only  $\sim 1\%$  of their candidates lie in the color-color space dominated by stars (stellar locus).

[Palanque-Delabrouille et al. \(2011\)](#) also used SDSS photometry to select AGN candidates through variability in the Stripe 82 field. On average, the light curves used by them had  $53 \pm 20$  epochs, and a total coverage between 4 and 10 years. They characterized the variability of each source using the structure function, and they classified the sources using a neural network algorithm. They applied their variability selection method to select candidates to be observed as part of the eBOSS survey. They demonstrated that their method is very efficient at selecting sources with  $z_{spec} > 2.2$  or BAL-QSO. However, the fraction of candidates with stellar-like colors is low (as can be seen in their Figure 18).

[Peters et al. \(2015\)](#) used SDSS data to perform a NBC KDE algorithm that classifies type 1 quasar, using color, variability and astrometric parameters. They used data in five broad optical bands (u, g, r, i, and z), and constructed light curves in each band with 10 to  $\sim 100$  observations over time-scales from  $\sim 1$  day to  $\sim 8$  years. They used structure functions to characterize the variability of each source. They tested different combinations of these parameters, finding that by combining variability and colors, they can achieve 97% efficiency, improving particularly the efficiency in the selection of quasars at  $2.7 < z < 3.5$ . They selected 35,820 type 1 quasar candidates, with only the 14% of them having  $g - r > 0.6$ .

More recently, [Tie et al. \(2017\)](#) combined colors and variability properties to select AGN candidates from DES. They obtained light curves from DES, which span less than a year and typically have  $\sim 15$  epochs. They

used the chi-squared integrated probability to select AGN candidates. Since they have light curves with only a year of coverage, they did not implement more sophisticated variability selection methods. They demonstrated that combining variability with optical and infrared photometry improves the efficiency of AGN selection. [Tie et al. \(2017\)](#) provide a catalog of 1,263 spectroscopically confirmed quasars in the DES supernova fields brighter than  $i = 22$  mag. Only 6% of their confirmed candidates have  $g - r > 0.6$ .

The light curves used in our analysis have a considerably higher cadence than the ones used in previous variability analyses, with an average of  $119 \pm 47$  epochs and a total length of  $1306 \pm 254$  days. In our case, we find that 39.1%, 31.2%, 18.7%, and 51.3% of the hp-AGN candidates from RF1, RF2, RF3, and RF4, respectively, have  $g - r > 0.6$ , where stars outnumber AGN. As we show in Section 4.2, most of the atypical AGN observed during our spectroscopic follow-up campaign lie in this region of color-color space (70% of the observed candidates). In general, our selection technique does not differ considerably to other techniques (e.g. [Palanque-Delabrouille et al. 2011](#); [Peters et al. 2015](#)). The key difference is the larger number of epochs and the larger coverage of the QUEST-La Silla light curves, in addition to the exclusion of morphological parameters during the selection of candidates. This help us to be more sensitive to atypical AGN, like BAL-QSO and LLAGN (observing four and eight, respectively, during the follow-up) compared with previous analyses, which might be related with the higher probability to detect a variable signal from our better quality light curves.

Our selection technique has the advantage of being easily applicable to LSST data, since the expected cadence for the DDF will be similar that the one used here ([LSST Science Collaboration et al. 2009](#)). LSST will provide multi-band light curves, which can help to weed out false positives and allow for a more complete characterization of the variability properties of the candidates.

## 6. CONCLUSIONS

We have presented a methodology to classify AGN through variability analyses, particularly useful to find AGN populations missed by other optical selection techniques. We used data from the QUEST-La Silla AGN variability survey to construct a total of 208,583 well-sampled light curves in the COSMOS, XMM-LSS, Elais-S1, and ECDF-S fields. We characterize the variability of these sources by using different variability features (see Section 3.2). We used a Random Forest algorithm to classify our objects as either AGN or non-



AGN using variability features and optical colors. We tested four classification schemes, one that includes only variability features (RF1), one that includes variability features and the  $r - i$  and  $i - z$  colors (RF2), one that includes variability features and the  $g - r$ ,  $r - i$ , and  $i - z$  colors (RF3), and another one that includes only optical colors. We have a total of 5,941 AGN candidates for the RF1 classifier, 5,252 candidates for the RF2 classifier, 4,482 candidates for the RF3 classifier, and 18,821 candidates for the RF4 classifier.

We confirmed the nature of our candidates by using ancillary data, and we found that a high fraction of the candidates from each classifier with  $g - r \leq 0.6$  are known AGN from the literature (52% for RF1, 52.4% for RF2, 52.1% for RF3, and 19.5% for RF4; see Section 4.1), but the fraction of candidates with  $g - r > 0$  confirmed by ancillary data is low (5.3% for RF1, 7.1% for RF2, 12% for RF3, and 1.6% for RF4). This is produced because most of the AGN known from the literature are biased against bluer optical colors by their selection criteria. This motivated us to perform spectroscopic follow-up, to confirm the nature of sources located in different regions of the color-color space.

We observed 54 candidates with EFOSC2/NTT and Goodman/SOAR, with 70% of the observed targets having  $g - r > 0$ . We confirm the nature of several interesting sources, including four BAL-QSOs, seven sources with  $z_{spec} > 2.5$ , and eight LLAGN. Our method was very efficient in classifying AGN with  $g - r \leq 0.6$ , for which we achieved 100% of efficiency for all the classifiers. For the case of sources with  $g - r > 0$ , our method also demonstrated good performance, achieving 73.7% efficiency for RF1, 79.4% for RF2, 85.2% for RF3, and 100% for RF4.

From the spectroscopic follow-up campaign, we conclude that the optimal classifier is the one that includes variability features and the  $r - i$  and  $i - z$  colors (RF2), as it avoids the region of the color-color space where we normally find cool stars, and also shows high efficiency, excluding only one observed type 1 AGN. The RF3 classifier also provides good results, however it excluded four AGN and one BAL-QSO. For the case of RF1, we propose that most of the candidates with  $g - r \sim 1.5$  and  $r - i \gtrsim 0.8$  are LPV or binary stars. The results of RF4 are very poor. It provides several hp-AGN candidates, but a low fraction of them are confirmed by the literature.

Our work can be considered as a pilot study in preparation for LSST, since the selection techniques tested here can be easily implemented for LSST data. The cadence of the LSST's DDF will be similar that the one of QUEST-La Silla, but covering 10 years of observations,

which will improve considerably the selection efficiency. In addition, LSST will provide observations in more than one photometric band, which might be useful to discard artifacts and false positives.

PS was supported by CONICYT through Beca Doctorado Nacional, Año 2013 grant #21130441. PS received partial support from Center of Excellence in Astrophysics and Associated Technologies (PFB 06). PL acknowledges Fondecyt Grant #1161184. NM acknowledges the support of the Helmholtz Einstein International Berlin Research School in Data Science (HEIBRiDS), Deutsches Elektronensynchrotron (DESY), and Humboldt-Universität zu Berlin. LCH was supported by the National Key R&D Program of China (2016YFA0400702) and the National Science Foundation of China (11721303). FEB acknowledges support from CONICYT-Chile (Basal AFB-170002) and the Ministry of Economy, Development, and Tourism's Millennium Science Initiative through grant IC120009, awarded to The Millennium Institute of Astrophysics, MAS. This work was partially funded by the CONICYT PIA ACT172033.

This work is based on observations obtained at the Southern Astrophysical Research (SOAR) telescope, which is a joint project of the Ministério da Ciência, Tecnologia, Inovações e Comunicações (MCTIC) do Brasil, the U.S. National Optical Astronomy Observatory (NOAO), the University of North Carolina at Chapel Hill (UNC), and Michigan State University (MSU).

Funding for the SDSS and SDSS-II has been provided by the Alfred P. Sloan Foundation, the Participating Institutions, the National Science Foundation, the U.S. Department of Energy, the National Aeronautics and Space Administration, the Japanese Monbukagakusho, the Max Planck Society, and the Higher Education Funding Council for England. The SDSS Web Site is <http://www.sdss.org/>.

The SDSS is managed by the Astrophysical Research Consortium for the Participating Institutions. The Participating Institutions are the American Museum of Natural History, Astrophysical Institute Potsdam, University of Basel, University of Cambridge, Case Western Reserve University, University of Chicago, Drexel University, Fermilab, the Institute for Advanced Study, the Japan Participation Group, Johns Hopkins University, the Joint Institute for Nuclear Astrophysics, the Kavli Institute for Particle Astrophysics and Cosmology, the Korean Scientist Group, the Chinese Academy of Sciences (LAMOST), Los Alamos National Laboratory, the Max-Planck-Institute for Astronomy (MPIA), the Max-

Planck-Institute for Astrophysics (MPA), New Mexico State University, Ohio State University, University of Pittsburgh, University of Portsmouth, Princeton Uni-

versity, the United States Naval Observatory, and the University of Washington.

## REFERENCES

- Abbott, T. M. C., Abdalla, F. B., Allam, S., et al. 2018, ArXiv e-prints, arXiv:1801.03181
- Abolfathi, B., Aguado, D. S., Aguilar, G., et al. 2018, ApJS, 235, 42
- Allevato, V., Paolillo, M., Papadakis, I., & Pinto, C. 2013, ApJ, 771, 9
- Bellm, E. 2014, in The Third Hot-wiring the Transient Universe Workshop, ed. P. R. Wozniak, M. J. Graham, A. A. Mahabal, & R. Seaman, 27–33
- Bertin, E., & Arnouts, S. 1996, A&AS, 117, 393
- Breiman, L. 2001, Machine Learning, 45, 5
- Butler, N. R., & Bloom, J. S. 2011, AJ, 141, 93
- Buzzoni, B., Delabre, B., Dekker, H., et al. 1984, The Messenger, 38, 9
- Caplar, N., Lilly, S. J., & Trakhtenbrot, B. 2017, ApJ, 834, 111
- Cardelli, J. A., Clayton, G. C., & Mathis, J. S. 1989, ApJ, 345, 245
- Cartier, R., Lira, P., Coppi, P., et al. 2016, The Messenger, 163, 26
- . 2015, ApJ, 810, 164
- Chen, C.-T. J., Brandt, W. N., Luo, B., et al. 2018, MNRAS, 478, 2132
- Clemens, J. C., Crain, J. A., & Anderson, R. 2004, in Proc. SPIE, Vol. 5492, Ground-based Instrumentation for Astronomy, ed. A. F. M. Moorwood & M. Iye, 331–340
- Covey, K. R., Ivezić, Ž., Schlegel, D., et al. 2007, AJ, 134, 2398
- Cristiani, S., Trentini, S., La Franca, F., & Andreani, P. 1997, A&A, 321, 123
- Croom, S. M., Rhook, K., Corbett, E. A., et al. 2002, MNRAS, 337, 275
- Doi, M., Tanaka, M., Fukugita, M., et al. 2010, AJ, 139, 1628
- Evans, P. A., Osborne, J. P., Beardmore, A. P., et al. 2014, ApJS, 210, 8
- Fan, X. 1999, AJ, 117, 2528
- Feruglio, C., Fiore, F., La Franca, F., et al. 2008, A&A, 488, 417
- Flesch, E. W. 2015, PASA, 32, e010
- Ginsburg, A., & Mirocha, J. 2011, PySpecKit: Python Spectroscopic Toolkit, Astrophysics Source Code Library, , ascl:1109.001
- Greene, J. E., & Ho, L. C. 2005, ApJ, 630, 122
- Gunn, J. E., Carr, M., Rockosi, C., et al. 1998, AJ, 116, 3040
- Ivezic, Z., Tyson, J. A., Abel, B., et al. 2008, ArXiv e-prints, arXiv:0805.2366
- Jones, D. H., Read, M. A., Saunders, W., et al. 2009, MNRAS, 399, 683
- Kelly, B. C., Bechtold, J., & Siemiginowska, A. 2009, ApJ, 698, 895
- Kelly, B. C., Becker, A. C., Sobolewska, M., Siemiginowska, A., & Uttley, P. 2014, ApJ, 788, 33
- Kim, D.-W., Protopapas, P., Bailer-Jones, C. A. L., et al. 2014, A&A, 566, A43
- Kim, D.-W., Protopapas, P., Byun, Y.-I., et al. 2011, ApJ, 735, 68
- Kim, M., Ho, L. C., & Im, M. 2006, ApJ, 642, 702
- Lacy, M., Storrie-Lombardi, L. J., Sajina, A., et al. 2004, ApJS, 154, 166
- Li, Z., McGreer, I. D., Wu, X.-B., Fan, X., & Yang, Q. 2018, ApJ, 861, 6
- LSST Science Collaboration, Abell, P. A., Allison, J., et al. 2009, arXiv e-prints, arXiv:0912.0201
- Luo, B., Brandt, W. N., Xue, Y. Q., et al. 2017, ApJS, 228, 2
- MacLeod, C. L., Ivezić, Ž., Kochanek, C. S., et al. 2010, ApJ, 721, 1014
- Maitra, C., Haberl, F., Ivanov, V. D., Cioni, M.-R. L., & van Loon, J. T. 2019, A&A, 622, A29
- Marchesi, S., Civano, F., Elvis, M., et al. 2016, ApJ, 817, 34
- McLaughlin, M. A., Mattox, J. R., Cordes, J. M., & Thompson, D. J. 1996, ApJ, 473, 763
- Medina, G. E., Muñoz, R. R., Vivas, A. K., et al. 2018, ApJ, 855, 43
- Myers, A. D., Palanque-Delabrouille, N., Prakash, A., et al. 2015, ApJS, 221, 27
- Nun, I., Protopapas, P., Sim, B., et al. 2015, ArXiv e-prints, arXiv:1506.00010
- Palanque-Delabrouille, N., Yèche, C., Myers, A. D., et al. 2011, A&A, 530, A122
- Peters, C. M., Richards, G. T., Myers, A. D., et al. 2015, ApJ, 811, 95
- Rahman, M., Mendez, A. J., Ménard, B., et al. 2016, MNRAS, 460, 163
- Richards, G. T., Fan, X., Newberg, H. J., et al. 2002, AJ, 123, 2945

- Richards, G. T., Myers, A. D., Gray, A. G., et al. 2009, *ApJS*, 180, 67
- Richards, J. W., Starr, D. L., Butler, N. R., et al. 2011, *ApJ*, 733, 10
- Ross, N. P., Myers, A. D., Sheldon, E. S., et al. 2012, *ApJS*, 199, 3
- Samus', N. N., Kazarovets, E. V., Durlevich, O. V., Kireeva, N. N., & Pastukhova, E. N. 2017, *Astronomy Reports*, 61, 80
- Sánchez, P., Lira, P., Cartier, R., et al. 2017, *ApJ*, 849, 110
- Sánchez-Sáez, P., Lira, P., Mejía-Restrepo, J., et al. 2018, *ApJ*, 864, 87
- Schlegel, D. J., Finkbeiner, D. P., & Davis, M. 1998, *ApJ*, 500, 525
- Schmidt, K. B., Marshall, P. J., Rix, H.-W., et al. 2010, *ApJ*, 714, 1194
- Schmidt, M., & Green, R. F. 1983, *ApJ*, 269, 352
- Secrest, N. J., Dudik, R. P., Dorland, B. N., et al. 2015, *ApJS*, 221, 12
- Sesar, B., Ivezić, Ž., Lupton, R. H., et al. 2007, *AJ*, 134, 2236
- Simm, T., Salvato, M., Saglia, R., et al. 2016, *A&A*, 585, A129
- Smartt, S. J., Valenti, S., Fraser, M., et al. 2015, *A&A*, 579, A40
- Smith, R. J., Croom, S. M., Boyle, B. J., et al. 2005, *MNRAS*, 359, 57
- Stern, D., Eisenhardt, P., Gorjian, V., et al. 2005, *ApJ*, 631, 163
- Tie, S. S., Martini, P., Mudd, D., et al. 2017, *AJ*, 153, 107
- van Dokkum, P. G. 2001, *Publications of the Astronomical Society of the Pacific*, 113, 1420
- Vanden Berk, D. E., Wilhite, B. C., Kron, R. G., et al. 2004, *ApJ*, 601, 692
- VanderPlas, J., Connolly, A. J., Ivezić, Z., & Gray, A. 2012, in *Proceedings of Conference on Intelligent Data Understanding (CIDU)*, pp. 47-54, 2012., 47-54
- VanderPlas, J. T. 2018, *ApJS*, 236, 16
- York, D. G., Adelman, J., Anderson, Jr., J. E., et al. 2000, *AJ*, 120, 1579

## APPENDIX

## A. CATALOG OF OBSERVED CANDIDATES

Here we present the list of candidates observed during our spectroscopic follow-up campaign. We provide the equatorial coordinates in degrees (J2000), telescope used, classifier from which the candidate was selected, measured redshift, quality flag of the measured redshift (1: low-quality  $z_{spec}$ , 2: good-quality  $z_{spec}$ ), the magnitude in the  $r$  band, the  $g - r$  color, the  $r - i$  color, and the spectroscopic classification. For details about the spectral analysis of these targets see Section B of the appendix.

**Table 8.** Targets observed during spectroscopic follow-up.

Name	RA	DEC	Telescope	Classifier	$z_{spec}$	FLAG <sub>z</sub>	$r$	$g - r$	$r - i$	Class
QLS_1	7.021016	-45.806145	SOAR	RF1/RF2	3.5852	1	20.14	1.13	0.31	AGN1
QLS_2	7.263506	-45.629417	NTT	RF1/RF2/RF3/RF4	1.3796	2	20.72	0.63	0.09	AGN1
QLS_3	7.323368	-43.633305	SOAR	RF1/RF2/RF3	0.3242	1	18.57	0.03	-0.08	AGN1
QLS_4	7.377026	-46.529945	NTT	RF1/RF2	0.2824	1	19.32	1.53	0.51	Gal
QLS_5	7.387083	-43.664276	NTT	RF1/RF2	0.2000	1	19.16	1.08	0.39	Gal
QLS_6	7.418616	-42.320072	NTT	RF1	0.0	2	17.88	1.52	1.24	STAR
QLS_7	7.419530	-43.789948	NTT	RF1/RF2	0.3912	2	18.91	1.12	0.34	AGN1
QLS_8	7.820146	-45.645706	NTT	RF1/RF2	0.3123	2	19.07	1.41	0.49	AGN1
QLS_9	7.970508	-42.275764	NTT	RF1/RF2/RF3	0.1847	2	18.02	0.99	0.41	AGN1
QLS_10	8.304768	-45.681595	NTT	RF1/RF2/RF3	0.2676	2	18.73	0.92	0.43	AGN1
QLS_11	8.348364	-46.856922	NTT	RF1/RF2/RF3	3.5297	2	19.90	0.75	0.08	AGN1
QLS_12	8.629325	-42.310108	SOAR	RF1	0.0	2	20.36	1.38	1.26	STAR
QLS_13	8.787973	-45.348194	NTT	RF1/RF2/RF3	0.1469	2	17.53	0.64	0.38	AGN1
QLS_14	9.407302	-43.000004	NTT	RF1/RF2/RF3	1.986	1	19.69	0.69	0.17	AGN1
QLS_15	9.414984	-43.422619	SOAR	RF1/RF2/RF3/RF4	1.8265	2	20.45	-0.06	0.29	AGN1
QLS_16	10.021671	-43.859173	NTT	RF1/RF2/RF3/RF4	0.3710	2	19.28	0.86	0.32	AGN1
QLS_17	10.097470	-44.866116	NTT	RF1/RF2/RF3	2.9609	1	19.94	0.70	0.38	BAL-QSO
QLS_18	10.225745	-43.855934	NTT	RF1/RF2/RF3/RF4	1.2671	1	20.49	0.63	-0.07	AGN1
QLS_19	10.758265	-42.452019	NTT	RF1/RF2/RF3	0.1000	1	19.90	0.89	0.24	Gal
QLS_20	10.866718	-43.825359	NTT	RF1/RF2/RF3	3.123	1	20.58	0.65	0.11	AGN1
QLS_21	11.090293	-43.665966	NTT	RF1/RF2/RF3	0.0	2	17.12	0.78	0.24	STAR
QLS_22	30.591522	-2.020991	SOAR	RF1/RF2/RF3/RF4	2.0502	2	18.66	0.04	0.11	AGN1
QLS_23	30.603312	-1.752825	NTT	RF1/RF2/RF3	0.2101	2	18.12	0.71	0.33	AGN1
QLS_24	31.057844	-2.953287	SOAR	RF1/RF2/RF3	0.1500	1	19.26	0.91	0.36	Gal
QLS_25	31.167528	-3.630512	NTT	RF1/RF2	1.22	1	19.14	0.61	0.06	BAL-QSO
QLS_26	31.533081	-2.510754	SOAR	RF1/RF2/RF3	1.4319	1	18.12	0.09	0.06	AGN1
QLS_27	32.158398	-3.652800	NTT	RF1	0.0	2	18.02	1.45	1.67	STAR
QLS_28	32.456287	-3.651828	SOAR	RF1/RF2/RF3/RF4	1.4976	2	18.85	0.09	0.14	AGN1
QLS_29	33.409081	-3.250347	SOAR	RF1/RF2/RF3	2.8491	2	19.54	0.16	0.06	AGN1
QLS_30	33.474072	-3.279924	NTT	RF1/RF3	0.5671	1	20.81	0.88	0.80	AGN1
QLS_31	36.426113	-2.971209	NTT	RF1/RF2/RF3	0.0	2	16.53	0.67	0.22	STAR
QLS_32	36.852539	-2.401858	NTT	RF1/RF2/RF3	0.2551	2	19.94	0.84	0.38	AGN1
QLS_33	37.988422	-2.585521	SOAR	RF1/RF2/RF3/RF4	0.3498	2	18.83	0.09	0.01	AGN1
QLS_34	38.680885	-2.637419	SOAR	RF1/RF2/RF3/RF4	0.8437	2	19.86	0.46	0.06	AGN1
QLS_35	51.529488	-29.656691	NTT	RF1/RF2/RF3	0.2307	2	18.15	0.87	0.43	AGN1
QLS_36	51.765114	-27.740358	SOAR	RF1/RF2/RF3/RF4	2.0279	2	19.20	0.07	0.17	AGN1
QLS_37	52.009411	-28.600405	NTT	RF1/RF2	0.2667	2	18.01	1.33	0.49	Gal

*Continued on next page*



Table 8 – *Continued from previous page*

Name	RA	DEC	Telescope	Classifier	$z_{spec}$	FLAG <sub>z</sub>	$r$	$g - r$	$r - i$	Class
QLS_38	52.013538	-30.619936	NTT	RF1/RF2/RF3	0.3284	2	19.47	0.90	0.37	AGN1
QLS_39	52.397503	-27.657492	NTT	RF1/RF2/RF3	1.4175	2	19.59	0.60	0.20	AGN1
QLS_40	52.536362	-29.822481	NTT	RF1/RF2/RF3/RF4	0.1804	2	17.51	0.66	0.53	AGN1
QLS_41	52.593563	-29.353525	NTT	RF1/RF2/RF3	0.2177	2	19.94	0.61	0.41	AGN1
QLS_42	53.317341	-29.488207	SOAR	RF1/RF2/RF3/RF4	1.9234	2	19.48	0.16	0.22	AGN1
QLS_43	53.730831	-27.736212	NTT	RF1/RF2/RF3	3.4986	1	19.37	0.86	0.27	BAL-QSO
QLS_44	53.749317	-27.499168	NTT	RF1/RF2	0.3598	2	19.42	1.13	0.40	AGN1
QLS_45	53.847992	-28.123224	SOAR	RF1/RF2/RF3/RF4	0.8682	2	17.11	0.09	-0.06	AGN1
QLS_46	53.864979	-26.950115	SOAR	RF1/RF2/RF3/RF4	0.8159	2	19.50	0.04	0.08	AGN1
QLS_47	53.911106	-28.961195	NTT	RF1/RF2/RF3	0.2116	2	18.54	0.72	0.46	AGN1
QLS_48	53.943211	-27.432163	NTT	RF1/RF2/RF3	0.4332	1	19.18	1.02	0.32	AGN1
QLS_49	54.049484	-28.095388	SOAR	RF1/RF2/RF3/RF4	2.5265	2	18.87	0.10	-0.04	AGN1
QLS_50	54.782047	-26.617104	SOAR	RF1/RF2/RF3/RF4	0.3825	2	19.14	0.70	0.26	AGN1
QLS_51	54.785744	-28.131121	SOAR	RF1/RF2/RF3	2.1388	1	19.20	0.34	0.09	BAL-QSO
QLS_52	54.878654	-27.307127	SOAR	RF1/RF2/RF3	1.0899	2	19.72	0.62	0.16	AGN1
QLS_53	55.059608	-26.485237	SOAR	RF1/RF2/RF3/RF4	1.6453	2	19.43	0.05	0.17	AGN1
QLS_54	149.004532	1.161204	SOAR	RF1/RF2/RF3/RF4	2.3530	1	20.36	0.33	0.09	AGN1

## B. SPECTROSCOPIC ANALYSIS OF THE OBSERVED CANDIDATES

We obtained classification spectra for 21 of our candidates using both the red and blue cameras of the Goodman spectrograph (Clemens et al. 2004), mounted on the SOAR telescope. We used the 400 lines mm<sup>-1</sup> grating and the 1.0" and 0.8" slits providing a typical resolution of  $\sim 6\text{\AA}$  or better. We reduced Goodman data following usual steps including bias subtraction, flat fielding, cosmic ray rejection (see van Dokkum 2001), wavelength calibration, flux calibration, and telluric correction using our own custom IRAF<sup>4</sup> routines.

We also obtained classification spectra for 33 candidates using EFOSC2 (Buzzoni et al. 1984) mounted on the New Technology Telescope (NTT) at La Silla Observatory. We used the 236 lines mm<sup>-1</sup> grating and the 1.0" slit providing a typical resolution of 18  $\text{\AA}$ . We followed the same observing procedures as the Public ESO Spectroscopic Survey for Transient Objects (PESSTO) collaboration (Smartt et al. 2015), using the PESSTO Observing Blocks (OBs) to perform our observations. We reduced our observations using the PESSTO pipeline (Smartt et al. 2015).

We corrected the reduced and calibrated one-dimensional spectra by Galactic extinction using the maps of Schlegel et al. (1998) and the model of Cardelli et al. (1989). We then computed their redshifts and spectral classes by cross-correlating every spectra with a set of spectral classification templates from SDSS<sup>5</sup>, a type 1 AGN composite spectrum (Croom et al. 2002), and a type 2 AGN spectrum (Jones et al. 2009). We define a redshift FLAG that indicates the quality of the measured redshift. We say that a computed redshift has good-quality (FLAG=2) when there are several lines in the spectrum, and these line are not affected by absorption features; and we say that a computed redshift has low-quality (FLAG=1) when the spectrum has low signal to noise, when the number of emission lines available is low (one or two), or when the emission lines are highly affected by absorption features. We measured the full width at half-maximum (FWHM) of the emission lines (when they were present) of each spectra, following a simple Gaussian fitting procedure with the *PySpecKit* Python package (Ginsburg & Mirocha 2011). The final classification of every source was done complementing the results of the cross-correlation analysis with visual inspection of every spectra. To distinguish type 1 and type 2 AGN, we requested that at least one emission line has FWHM  $> 1800$  km/s in the rest-frame. In Figure 10 we provide the rest-frame optical spectra of our 54 candidates.

<sup>4</sup> IRAF is distributed by the National Optical Astronomy Observatories, which are operated by the Association of Universities for Research in Astronomy, Inc., under cooperative agreement with the National Science Foundation.

<sup>5</sup> <http://classic.sdss.org/dr5/algorithms/spectemplates/>

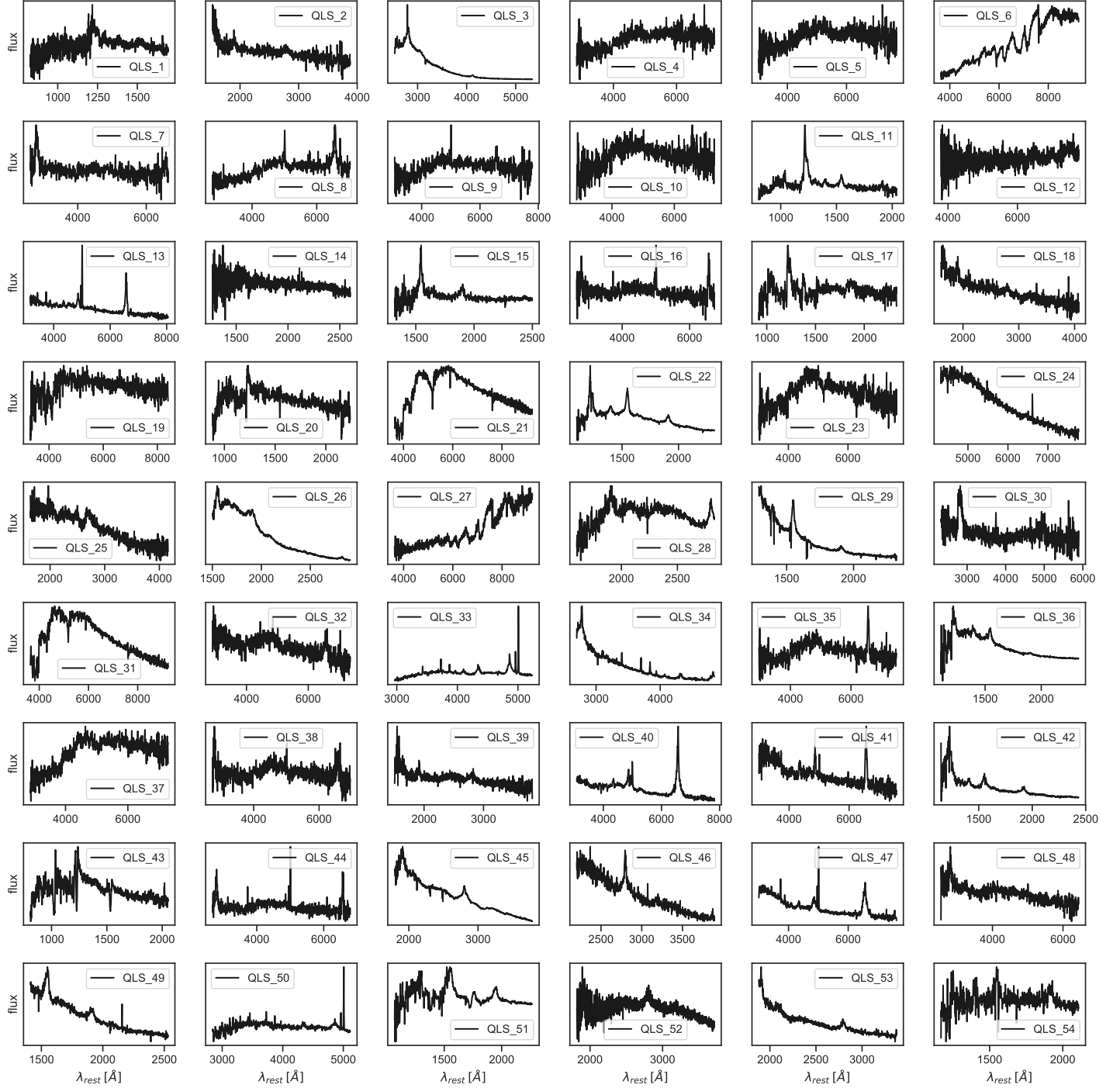


**Figure 10.** Rest-frame optical spectra of the observed candidates. The flux is in arbitrary units.

### C. HP-AGN CANDIDATES FROM THE RF2 CLASSIFIER

In Table 9 we show the list of hp-AGN candidates selected using the RF2 classifier. We provide the equatorial coordinates in degrees (J2000), the  $r$  band magnitude, the  $g-r$  and  $r-i$  optical colors, the most relevant variability features of RF2 ( $A_{SF}$ ,  $\sigma_{rms}$ ,  $Q31$ , and  $P_{var}$ ), the predicted class, and the predicted class probability ( $P_{RF}$ ).

**Table 9.** List of hp-AGN candidates selected by the RF2 classifier

RA	DEC	$r$	$g - r$	$r - i$	$A_{\text{SF}}$	$\sigma_{\text{rms}}$	Q31	$P_{\text{var}}$	class	$P_{\text{RF}}$
148.314270	2.172078	20.30	0.72	0.32	0.002	4.547e-6	0.127	0.946	AGN	0.86
148.396057	0.476811	18.22	0.41	0.14	0.107	1.323e-6	0.105	0.999	AGN	0.91
148.432525	1.672532	17.62	0.37	0.15	0.069	-3.904e-6	0.088	0.967	AGN	0.82
148.497756	0.645931	19.79	0.22	0.31	0.239	1.555e-5	0.189	1.000	AGN	0.99

**Note.** Only a portion of this table is shown here to demonstrate its form and content. A machine-readable version of the full table is available.